MASS SPECTROMETRIC STUDIES OF IONIZATION PRECURSORS AHEAD OF STRONG SHOCK WAVES

Thesis by

William M. Robinson, Jr.

In Partial Fulfillment of the Requirements

For the Degree of

Doctor of Philosophy

California Institute of Technology

Pasadena, California

1969

(Submitted May 29, 1969)

ACKNOWLEDGEMENTS

The author wishes to express his sincere appreciation to his advisor, Professor Hans W. Liepmann, whose enthusiasm and guidance served as a constant source of motivation and inspiration. The contributions and advice of Professor Bradford Sturtevant helped considerably to make the present work possible. His patient suggestions of how to translate the manuscript from Southern into English are gratefully appreciated.

The author wishes to thank Mr. Brian Barcelo for designing and constructing the piezoelectric gauge and for his aid in preparing the manuscript. Special thanks go to Mrs. Jacquelyn Beard for typing the manuscript.

The author is indebted to the California Institute of Technology and the National Aeronautics and Space Administration for their financial assistance. The work in the GALCIT 6" shock tube was supported by the National Aeronautics and Space Administration.

The deepest appreciation of all is felt for the author's wife, Jeanne, for her encouragement, sacrifice, and understanding during the difficult years.

ABSTRACT

An experimental study was conducted to identify the nature and origin of precursor ions produced by photoionization ahead of strong shock waves in xenon. A magnetic mass spectrometer is mounted at the end of a hydrogen-driven shock tube. Ions produced upstream of a shock wave are sampled by the spectrometer and the collected current provides a continuous time history of a particular ionic species. A mass spectrum is obtained in the precursor region for all impurities found in the shock tube. The incident shock Mach number is varied from 11.9 to 21.3, the initial pressure is varied from 0.050 to 0.500 torr, and the impurity level is altered. In all the conditions studied, the dominant ion present in the precursor is Xe^+, although in certain instances, the impurity ion currents are found to be of the same order of magnitude as the xenon ion current. For small impurity levels, photoionization processes in xenon and impurities are apparently independent. Independent double probe measurements determine the total ion density to be about 10^{12} cm^{-3} at the shock front, the observable precursor extending about 150 cm from the shock wave.

A theoretical model accounting for one-step and multistep photoionization of xenon and impurities is used to find the ionization level ahead of a shock wave. The

calculated ion density profiles agree well with experimental observations at the low pressures, where it appears that one-step photoionization predominates. Lack of agreement at high pressures, where, apparently, multi-step ionization is more efficient than the single-step process, suggests inadequacies in the treatment of photoexcitation and multi-step photoionization. Additional areas for experimental study are suggested.

The mass spectrometric data yield a better understanding of the role of radiation in shock structure, of the kinetics of photoionization processes in rare gases, and of the influence of impurities in the experimental facility on the radiation mechanisms.

TABLE OF CONTENTS

PART	TITLE	PAGE
	Acknowledgements	i
	Abstract	ii
	Table of Contents	iv
	List of Figures	vii
I.	Introduction	
	1.1 Motivation for the Study of Precursors	1
	1.2 Previous Theoretical and Experimental Studies	2
	1.3 Aim of the Present Experimental Technique	7
II.	Description of the Experimental Apparatus	11
	2.1 Brief Description of the Shock Tube	11
	2.2 The Mass Spectrometer	13
	2.3 The Langmuir Double Probe	14
III.	Experimental Results	16
	3.1 Measurement of the Total Ion Density of the Double Probe	16
	3.2 Precursor Ionic Products in "Pure" Xenon	18
	3.3 Effect of Impurities on Precursors	22
	3.3a Naturally-Occurring Impurities	22
	3.3b Added Impurities	23
	3.3c Impurities in the Driver Section	25
	3.4 Experiments in Argon	25
IV.	Theoretical Results	27
	4.1 One-step Photoionization of Xenon and Impurities	28
	4.2 Multi-Step Photoionization of Xenon	30
V.	Discussion and Comparison of the Experiment and Theory	32

TABLE OF CONTENTS (cont.)

PART	TITLE	PAGE
	5.1 Photoionization at Low and High Initial Pressures	32
	5.2 Precursor Dependence on Shocked Gas Temperature	33
	5.3 Discussion	34
VI.	Conclusions	40
Appendices		
A.	The GALCIT 6" Shock Tube	42
	A.1 Description of the Basic Shock-Tube System	42
	A.2 Operating Conditions and Limitations	45
	A.3 Determination of Shock Wave Velocity and Position	46
	A.4 Measurement of Initial Pressure and Impurity Level	48
	A.5 Natural Impurities Present in the 6" Shock Tube	50
	A.6 Pressure Relief System for the 6" Shock Tube	51
B.	The Mass Spectrometer as a Diagnostic Tool	54
	B.1 Physical Characteristics of the Spectrometer	55
	B.2 Operating Conditions and Limitations of the Mass Spectrometer	59
	B.3 Mass Spectrometer Calibration	62
C.	The Langmuir Double Probe	65
	C.1 The Langmuir Double Probe as a Diagnostic Tool	65
	C.2 Description of the Probe and its Application	67
	C.3 Measurement of Number Density with a Mexican Radio Station	69
D.	Typical Experimental Procedure	76
E.	Theory of Photoionization	79
	E.1 Ionization Ahead of a Strong Shock Wave	79
	E.2 One-Step Photoionization of Xenon and Impurities	83

TABLE OF CONTENTS (cont.)

PART	TITLE	PAGE
	E.3 Photoexcitation and Multi-Step Photo-ionization of Xenon	88
	References	98
	Tables	102
	Figures	103

LIST OF FIGURES

1. Schematic Diagram of the Apparatus

2. GALCIT 6" Shock Tube Test Section

3. Mass Spectrometer Installation at the End of the Shock Tube

4. Mass Spectrometer Installation

5. Schematic Representation of a Mass Spectrum of Impurities in the 6" Shock Tube

6. Langmuir Double Probe Schematic

7. Probe Ion Current Profiles Showing the Effect of Variation of Impurity Levels

8. Probe Ion Current at a Distance of 5 cm as a Function of Equilibrium Temperature behind the Shock

9. Comparison of Ion Number Density Determined from Double Probe Currents and Xenon Ionic Currents Obtained from Mass Spectrometric Data for Two Different Initial Pressures

10. Schematic of Probe-Measured Ion Density and Spectrometer-Collected Ion Currents as a Function of Distance from the Shock Wave (Low Pressure)

11. Schematic of Probe Measured Ion Density and Spectrometer-Collected Ion Currents as a Function of Distance from the Shock Wave (High Pressure)

12. Comparison of One-Step Photoionization Theory with Maximum Spectrometer Currents for Injection of Molecular Oxygen and Nitrogen in Pure Xenon

13. Spectrometer Oscillograms Showing Decrease in Xenon Current Due to Addition of Large Amounts of Impurities

14. Argon Ionic Current Collected by the Spectrometer

15. Simplified Schematic of Xenon Energy Levels and Rates

16. Shock Tube Radiation Model in Shock-Fixed Coordinates

17. Comparison between Experimental Spectrometer Measurements and One-Step Photoionization Theory for Low Initial Pressure

LIST OF FIGURES (cont'd.)

18. Comparison between Experimental Spectrometer Measurements and Theory for High Initial Pressure

19. Profile Comparison between One-Step Photoionization Theory and Double Probe Data as a Function of Temperature behind the Shock

20. Schematic of Piezoelectric Detector

21. Typical Piezoelectric Crystal and Thin-Film Resistance Gauge Oscillograms

22. Typical Spectrometer Oscillograms Showing the Method of Data Reduction

23. Typical Double Probe Response Showing Localized Perturbation

24. Double Probe Response Showing Localized Perturbation with Fast-Rise-Time Circuitry

25. Shock Tube and Associated Equipment Ground Reference

26. Detail of Probe Perturbation Showing Modulations and High Frequency Components

27. Comparison of Spectrometer Current Using Semi-Empirical Calibration and Probe Current Using Ion Resonance as Reference

I. INTRODUCTION

The presence of electrically-charged particles in the undisturbed gas ahead of strong shock waves has recently been the subject of intense study; the ions and electrons are called "ionization precursors". Such precursors are observed in experimental facilities generating strong shock waves. There exists strong experimental evidence that the ionization is due to the propagation of radiant energy into the region ahead of the shock, although difficulties are encountered in theoretically predicting the precursor ionization levels due to photoionization.

1.1 Motivation for the Study of Precursors

There is no doubt that as shock-wave strengths increase, the effect of radiation from the shocked gas must be considered. Large radiant fluxes may propagate ahead of the shock wave and preheat or ionize the undisturbed gas. Under these conditions the gas behind the shock front loses energy and is thereby radiatively cooled, while the shock wave is propagating into an ionized plasma instead of a cold gas. The result is a modification of the flow conditions in the shocked gas.

Thus, for strong shock waves the precursor becomes a part of the total shock structure, and a knowledge of precursor properties is mandatory. A study of precursors is desirable not only in understanding the effect of

radiation kinetics on reactions in shock heated flows in experimental facilities, but because closely related effects may occur in practical hypervelocity problems such as spacecraft re-entry (see for example, reference 1). The propagation of electromagnetic radiation in the vicinity of a re-entry body would certainly be affected by the ionization level surrounding it.

1.2 Previous Experimental and Theoretical Studies

The first manned orbital re-entry by the MA-6 Mercury capsule in 1962 offered a possible observation of precursors in the leading edge radar echoes. Apparently the ultraviolet radiation from the high temperature region behind the bow shock wave of the blunt-nosed body ionized the cold gas ahead sufficiently to reflect radar signals from the ground. The precursor ionization level was sufficient to return radar echoes at altitudes far in excess of where the physical dimensions of the capsule would have returned them. Lin, et. al. (Ref. 2), calculated the electron number density from photoionization to be $\sim 10^{7}$ cm^{-3} at a mean radial distance of 18 meters from the bow shock. This phenomena was observed at an altitude of 220,000 feet (pressure $\sim$ 0.100 torr) with a capsule velocity of 7×10^{5} cm/sec ($M_s \sim 25$).

Precursors experimentally studied in conventional pressure-driven shock tubes have been attributed to three

possible mechanisms: 1) photoemission from the shock tube walls and instrumentation 2) diffusion of charged particles from the hot region behind the shock 3) photoionization by strong radiation from behind the shock wave. Several experimental studies in argon and xenon at high Mach numbers were conducted in various shock tube facilities and differing results were obtained. Hollyer (Ref. 3) investigated the effect with biased probes and concluded that photoemission and impurity level were very important. In some of the experiments, he found both ions and electrons present ahead of the shock. Groenig (Ref. 4), using a spark discharge probe, and Weymann (Refs. 5,6) using potential probes, electrostatic probes, and induction coils, found that electron diffusion from behind the shock was the dominant mechanism. Gloersen (Ref. 7), using potential probes, found all three mechanisms present and determined that the introduction of impurities caused inconsistant results.

More recently, Holmes (Ref. 8) using collecting probes and potential probes, found equal electron and ion density profiles ahead of the shock wave, implying the predominance of photoionization. Using argon (2-10 torr) as the test gas and a Mach number range of 9-11, he found ion number densities up to 10^{12} cm^{-3} at the shock front. Measurable ionization levels were found up to 160 cm in front of the shock.

Lederman and Wilson (Refs. 9, 10) conducted high Mach number experiments in argon in a small diameter shock tube, using tuned microwave cavities. For similar conditions, their measured precursor ionization levels were lower than Holmes', implying that shock tube geometry may be important. Using first a biased electrostatic grid to contain diffusing electrons and then an opaque radiation block with obliquely drilled holes to allow diffusion, they concluded that at least for their conditions, photoionization was the major cause of precursor ionization. They found that the injection of rather large amounts of hydrogen as an impurity appreciably changed the precursor characteristics.

Precursors in electromagnetic shock tubes have been observed and reported in the literature. These shock tubes have large amounts of radiation and induced electromagnetic effects emanating from the initial electrical discharge. A study using a combustion-driven shock tube (Ref. 11) reported spurious signals during ignition of the driver. The results of these experiments were excluded from consideration here due to the shock tube driver technique further complicating measurements of the precursor phenomena.

Of the three possible mechanisms for the explanation of ionization ahead of shock waves, i.e., electron diffusion, photoionization, and photoemission, the first two

have received considerable theoretical attention. Several analyses (Refs. 12, 13, 14) of the electron diffusion model have been made, using different electric field distributions in the shock wave (due to charge separation) and various models for electron production. All investigations mentioned the strong inhibiting electric field arising from the fast diffusion of electrons away from the less mobile ions (ratio of diffusion coefficients for electrons and ions is inversely proportional to the square root of their mass ratio). The general conclusion was that electron diffusion may be neglected for distances greater than one Debye length ahead of the shock wave, an insignificant distance in comparison with experimental observations.

Ferrari and Clarke(Ref. 15) theoretically treated the photoionization problem. Assuming one-step photoionization as the dominant mechanism, their results showed almost negligible ionization in comparison to the experimental observations in argon.

Wetzel (Ref. 13) found that radiation of sufficient energy to photoionize argon from the atomic ground state decayed much too rapidly to explain the observed ionization profiles. Holmes (Ref. 8) has suggested that radiation processes involving one or more absorption steps to populate higher excited states prior to photoionization may significantly increase the precursor levels predicted by theory. Murty (Ref. 16), Biberman and Veklenko (Ref. 17),

and most recently Dobbins (Ref. 18) have studied the role of line radiation and "radiation trapping" in ionization processes ahead of strong shock waves. Their results also failed to predict the observed ionization levels.

Dobbins gave specific consideration to shock tube geometry and the physical characteristics of the problem (e.g., length of the radiating volume of shocked gas, reflection of the shock tube walls, etc.) This aspect of his work was especially important in view of the fact that most of the previous theoretical investigations assumed a one-dimensional model. In all of the experimental work reported, the shock tube diameter was less than two inches. Correlating a theoretical radiation model with a small geometry was very difficult. Dobbins' axially-symmetric treatment is relevant in the present experiment since the shock tube radius is much larger than those used in previous studies and in the present work a discontinuous change of diameter occurs in the shock tube (see Appendix B.1).

Appleton (Ref. 14) and Wilson and Lin (Ref. 19) found that photoionization of small amounts of impurities present in a shock tube might explain the magnitude of ionization experimentally observed. The lower number densities and smaller photoionization cross sections of various impurity gases suggested longer mean free paths than those in argon,

so the decay rate of the electron and ion profiles for one-step photoionization is not large in some cases.

The diagnostics used in all of the previous studies were such that only the total electron density or current and the total ion density could be observed. Insight into the basic experimental problem could not be gained until the relative magnitudes of the independent parameters, such as impurity level, could be isolated and studied separately. The main conclusions that may be drawn from the literature were that for the case of strong (i.e., $M_s > 10$) shock waves, the precursor was dominated by photoionization, and that the impurity level was of extreme importance. Of the theoretical analyses that have been made, all predicted ionizational levels orders of magnitude lower than the pertinent experimental results.

1.3 Aim and Methods of the Present Experiments

In earlier studies, conventional probe and microwave diagnostics produced differing results depending on the experimental facility used, implying that the observations may be impurity dominated. These studies emphasized the complexity of observing the precursor phenomena, and sometimes made it doubtful as to what was being studied, photoionization of a pure, noble gas, photoionization of impurity gases, or some combination of both. The presence

of impurities are a consequence of the interferences of the experimental facility.

It is well known that impurities can appreciably alter and sometimes dominate the shock-wave characteristics, such as relaxation time, in a shock tube (for example see references 20 and 21). The conflicting experimental data and the fact that some impurity gases have longer radiation mean free paths than the noble gases emphasizes the importance of studying the role of shock-tube impurities in the precursor. Since photoionization has the property of producing free ions at large distances from the shock wave, and identification of these ions would give insight as to the nature and origin of the precursor ionization, a mass spectrometer is used to examine the precursor region. This diagnostic tool allows an uncoupling or separation of the mechanisms influencing shock structure in the "pure" test gas from the effect of various foreign gases in the test facility itself. Individual effects, species by species are, examined and in this manner the total effect is deduced.

A schematic of the apparatus is shown in figure 1. The GALCIT* 6" shock tube is used to reproducibly generate strong normal shock waves. A magnetic mass spectrometer is mounted on the shock tube end wall, sampling ions from a region on the axis of the shock tube. Ions produced

---

*Graduate Aeronautical Laboratories, California Institute of Technology

upstream of the approaching shock wave are sampled by the spectrometer and the collected current provides a continuous time history of a particular ionic species. Assuming a constant shock velocity U_s in the observation time t, the current history becomes a spatial profile of ion density ahead of the shock wave through the transformation $x = U_s t$. A complete mass spectrum is obtained by duplicating runs with the spectrometer set at different mass peaks. Dominant impurities in the shock tube are determined and the relative abundance of the individual ions are surveyed under a variety of test conditions. The incident shock Mach number is varied from 12 to 21, the initial pressure is varied from 0.050 to 0.500 torr, and the impurity level is altered. To obtain a quantitative estimate of the ionization levels and to check the overall repeatability of the shock conditions, an electrostatic ion collecting probe is used.

A theoretical model of the radiation processes is compared with the experimental results. The geometry of the large radius shock tube used in the present investigation should be more applicable to treatment by theoretical considerations since it is difficult to establish a correct radiation model for the shocked gas in a constricted geometry such as a small radius shock tube. Gaining insight from the experimentally-determined behavior of the

most fundamental property of the precursor, i.e., the relative abundance of its constituents, the experimental conclusions may be used to locate aspects of the theory that are incomplete and to determine the accuracy of theoretical assumptions. Identification of the correlation between theory and experiment leads to the prediction of the relative importance of precursors in the rest of the shock structure and to appropriate aims for further study.

II. DESCRIPTION OF THE EXPERIMENTAL APPARATUS

2.1 Brief Description of the Shock Tube

The experiments were performed in the GALCIT 6" diameter shock tube (see figures 1, 2). A more complete description of which is given in Appendix A and reference 22. The essential advantages of this shock tube for the present investigation are: a) its low leak rate and evacuation capabilities which permit the impurity levels in the test gas to be controlled, b) its unique diaphragm-opening mechanism, the use of which results in reproduction of shock strength to an accuracy of $\pm$1%, and c) its previously determined characteristics (e.g., ionizational equilibrium relaxation times) for use in theoretical calculations (see reference 23).

The stainless steel tube consists of a 6" I.D., low pressure test section, 37' long and honed internally to a mirror finish, and a 6.5" I.D. driver section, 6.5' long. In the present investigation, room temperature hydrogen or helium is used as the driver gas to produce incident shock Mach numbers ranging from 11.9 to 21.3 in xenon (a limited number of experiments were also conducted in argon). The initial pressure of xenon is varied from 0.05 to 0.5 torr.

The high Mach numbers which can be attained in xenon, due to its low speed of sound, together with xenon's lower ionization potential, results in much higher degrees of

ionization than would have been attained in argon at the same initial pressure. Obtaining precursor ionization levels in argon within the sensitivity of the spectrometer requires high driver pressures. This results in final shock tube pressures too high for the mass spectrometer orifice diaphram and slide valve (see Appendix B). Lower cost of production of xenon in recent years and very recent experimental studies of the properties of xenon permit its use in the present investigation.*

The vacuum system consists of mechanical pumps in series with a liquid nitrogen cold-trapped oil diffusion pump (ultimate pressure 7×10^{-6} torr; initial combined leak and outgassing rate 1.7×10^{-3} torr/hr). A McLeod gauge is used as a reference for a thermocouple gauge and a cold-cathode ionization gauge which continuously monitor the vacuum level during pumping. The primary gas is introduced from a calibrated volume within seconds after closing the diffusion pump. Impurities are introduced through a calibrated volume or by allowing the test section to leak to the desired level. A bellows-type pressure gauge is used to measure the pressure in the small control volume.

---

*The cost for one shock tube experiment in xenon at an initial pressure of 0.1 torr, including diaphragm and hydrogen driver gas, is less than $2.00.

The incident shock velocity and position are determined to $\pm$1% by observing the responses of two platinum thin film heat transfer gauges and an electrostatically-shielded piezoelectric crystal mounted adjacent to the mass spectrometer.

With the mass spectrometer ion source connected directly to the shock tube test section, the abundance of "naturally occurring" (due to leaks and out-gassing) impurities is determined. The predominant impurities are N_2, H_2O, O_2, and several groups of organic compounds, in decreasing abundance.

2.2 The Mass Spectrometer

A modified Nier-type magnetic mass spectrometer* is mounted on the end wall of the shock tube (see figures 3, 4). Ions produced by photoionization in front of an approaching shock wave are sampled through small orifices in the end wall and the measured currents provide a continuous time history of a particular ion with micro-second resolution, i.e., the ion abundance as a function of distance from the shock wave. High mass resolution and extremely fast time-response are obtained by observing the time history for only one mass peak during each run.

---

*A more complete description of the mass spectrometer and its application is given in Appendix B and reference 20.

On the other hand, several runs are required to obtain the complete spectrum, making duplication of experimental conditions very important. The mass resolving power of the spectrometer is variable from 1 in 10 to 1 in 200, and ion densities greater than 10^9 cm^{-3} in the shock tube can be detected.

In the present shock tube experiments, the impurity levels, the initial pressure and the Mach numbers are systematically altered. The relative abundance of individual ions in the precursor region of the shock wave are surveyed under a variety of test conditions. By determining the efficiency of the sampling process, a calibration constant is obtained for the spectrometer, relating the collected ion current with a particular ion number density in the shock tube during an experiment.

An external ion source which is used to set the particular mass number peak before each run (see Appendix D) also determines the dominant impurities in the shock tube. (see figure 5). The spectrum scan is obtained by continuously altering the spectrometer magnetic field strength while observing the collected ionic current.

2.3 The Langmuir Double Probe

To obtain a quantitative estimate of the ionization levels, an electrostatic double probe (see Appendix C) which floats at plasma potential is biased at a potential

difference which assures positive-ion-current saturation (see figure 6). The probe system consists of two wires extending into the test section in a plane perpendicular to the axis of the shock tube. Assuming that the ionic current falling on the probe is characteristic of the random thermal motion in the gas ahead of the shock wave, the current in the negatively biased probe is directly related to the ion density in the test section. The initial test pressures in the present experiments are such that the criterion for the free molecular flow model of the probe current collection should be reasonably well satisfied. The mass of the predominant ion collected by the probe is determined by the mass spectrometer.

Observation of the total ion current collected during each run assures repeatability of precursor ionization levels while the individual currents are collected by the spectrometer. The double probe is used to monitor the precursor ionization in different regions of the shock tube as well as in the spectrometer sampling position. Probe orientation is varied to determine the effect of photo-emission from the probe surface (see Appendix C.2). Under particular operating conditions, an interesting resonance phenomenon is observed, which leads to a further independent determination of number density. This effect is described in detail in Appendix C.3.

III. EXPERIMENTAL RESULTS

The precursor ionization levels are sufficiently high to provide measurable spectrometer ion currents in "pure" xenon. The relative abundance in the precursor of the individual shock-tube impurities under a variety of test conditions is determined.

Examination of the experimental data shows that insight into the fundamental problem may be gained by comparing two precursor profiles that exemplify contrasting features. The precursor data may be grouped into low and high-pressure regimes.

The gross features of the precursor will be qualitatively described first. Then the mass spectrometric results for the two pressure divisions will be given, followed by a discussion of the role of impurities on precursors. The abundance of impurities in the present section are determined by the partial pressure of "naturally-occurring" foreign gases, unless otherwise noted.

3.1 Measurement of the Total Ion Density with the Double Probe

During each run, a measurement of the total ion density is made concurrently with the spectrometer measurement. In this manner the repeatability of the precursor characteristics could be checked from run to run while the

spectrometer samples separate mass peaks. In general, if a strict procedure is followed for a series of runs, the total ion density measurements are quite reproducible. The double probe is useful for exhibiting the gross behavior of the precursor because with the spectrometer this would require several measurements.

Typical probe ion currents observed during experiments to demonstrate the effect of the injection of impurities are shown in figure 7. Changing the impurity levels results in small variations as compared to the total ion currents collected. At impurity levels greater than about 1%, the precursor characteristics show distinct alterations, such as a complete lack of precursor; thus impurity concentrations above this level are not considered (see part 3.3).

The probe is also used to determine the dependence on particular parameters in the experiments. It is not apparent what choice of independent parameters best exhibits the nature of the precursor. The two major factors that must be considered are initial pressure, i.e., neutral atom number density in the cold gas, and shock wave Mach number. The first determines the photon mean free path in the absorbing gas, and the second primarily determines the temperature in the equilibrium zone and hence, the radiant energy available for photoionization.

Holding the Mach number constant and varying the initial pressure will not merely change the radiation mean free path since variation of pressure also changes the equilibrium temperature. Keeping the initial pressure constant and varying the Mach number, on the other hand, should show the dependence of the precursor on the equilibrium temperature of the shocked gas. Figure 8 shows a semilogarithmic plot of the probe ion current, at a distance of 5 cm from the shock wave, versus the equilibrium temperature. A comparison will be made in Part 5.2 between this plot and a theoretical calculation of one-step photoionization.

3.2 Precursor Ionic Products in "Pure" Xenon

The various ionic products produced by photoionization ahead of strong shock waves in "pure" xenon, including impurities introduced by the experimental facility, are measured with the mass spectrometer. A large number of different ions are observed, with Xe^+ ions predominating under all conditions.

The parameter which produces the largest variation in the precursor behavior is the initial pressure of xenon. As the initial pressure increases, the characteristics of the precursor change substantially. The spectrometrically-obtained xenon ion currents for initial pressures of 0.120 and 0.500 torr are presented schematically in figure 9.

For comparison, the ion density profiles (dashed lines) determined from the double probe currents are shown for the same conditions. The probe current tends to follow the xenon ion current for both cases. The impurity levels refer to the abundance of "naturally-occurring" impurities, i.e., impurities resulting from test section leak and outgassing.

In general, at low initial pressures ($P_1 \sim 0.100$ torr) as the Mach number and shocked gas equilibrium temperature increase, so does the impurity ionization. Below Mach numbers $M_s \sim 13$, all impurity currents are below the sensitivity limit of the spectrometer. The higher the initial pressure of xenon, the greater the ratio of xenon to impurity ionic currents, implying that the contributions to the precursor of the individual species are uncoupled and proportional to their partial pressures. The use of the mass spectrometer in the present application then allows measurements to be made of impurity effects and of photoionization in the xenon.

The results of a series of runs at a particular impurity level are shown in figure 10. The solid lines are the ion currents collected by the mass spectrometer. The dashed line is again the total ion number density as measured by the double probe. The conditions considered in figure 10 are in the low pressure range where impurity

ionization is of the same order of magnitude as the xenon ionization. The group of ions with mass numbers 68-71 amu is the dominant impurity in the precursor, although it is not the most abundant impurity in the shock tube before each run (see figure 5 and Appendix A.5). Some small amounts of ionization products with mass numbers of 1 (H^+) , 16 (O^+) , 65-67 (Xe^{++}) and 57 amu , but no discernible amounts of 2 (H_2^+) and 18 amu (H_2O^+) are observed. Consequences of varying the impurity levels will be described in the following section.

Ions with mass 65-67 amu , possibly attributable to doubly-ionized xenon, are detected at the higher Mach numbers ($M_s > 17$) . The abundance of the predominant isotopes of xenon are given in the following table (Ref. 24).

Isotope	% Natural Abundance
Xe^{129}	26.24
Xe^{131}	21.24
Xe^{132}	26.93
Xe^{134}	10.52
Xe^{136}	8.93

Doubly-ionized Xe^{132} , Xe^{134} , Xe^{136} have mass numbers (66, 67, 68 amu) located in close proximity to impurity ions observed in the shock tube (see figure 5). To separate the Xe^{++} ionic currents from these impurity

currents, the test section is evacuated to a pressure below which negligible impurity currents are collected by the spectrometer. The measured currents at these mass numbers do not change with impurity level, implying they are related only to the xenon atoms present, i.e., Xe^{++}.

The effect of increasing the initial pressure is shown in figure 11. At this high pressure, xenon ionization completely prevails over impurity ionization far ahead of the shock wave as well as near the wave. Xenon ions are detected up to 120 cm from the shock wave. Typical impurity ion profiles are shown for two different impurity levels. In comparison with figure 10, the magnitudes of the impurity ionization levels are about the same as at lower initial pressures, showing the radiation mechanism in the impurity photoionization process has not basically changed; only the xenon ionization level shows a behavioral change, e.g., a change in slope at distances far from the wave. Sampling limitations imposed by the mass spectrometer preclude the study of pressures $P_1 > 0.500$ torr (see Appendix B.2); however, no major changes in the basic precursor structure are anticipated for higher pressures. Xenon ionization should be much larger than impurity ionization.

3.3 Effect of Impurities on Precursors

3.3a Naturally-Occurring Impurities

At low pressures ($P_1 \sim 0.100$ torr xenon) the presence of small amounts of impurity gases in the shock tube test section results in impurity ionization levels of the same order of magnitude as the xenon levels in the precursor. As the initial pressure of xenon increases, the role of impurities in the precursor becomes negligible in comparison to that of xenon (Fig. 11). The effect of varying the impurity levels in low-initial-pressure xenon experiments will now be qualitatively described.

As discussed in Appendix A.4 the "naturally-occurring" impurity level for each run is calculated from the degassing rate and the time elapsed between closing the diffusion pump valve and bursting the shock tube diaphram. Allowing longer elapsed times between closing the pump and firing causes the partial pressures of the main constituents of air to increase while the other impurity levels remain fairly constant, as would be expected from leakage in the shock tube test section (see Appendix A.5). The behavior of the O_2^+ and N_2^+ ion currents in the precursor for a variation in naturally-occurring impurity levels will be discussed in Part 3.3b.

For variation in natural impurity levels of from 0.1 to 1%, the 68-71 amu ionic currents collected by the spectrometer during a run remain fairly constant.

Lowering the impurity level from 0.1 to 0.05% results in a decrease in the current of this group of impurities, until the ion density level is below the sensitivity of the mass spectrometer. This group of organic ions in the precursor is probably attributable to oils in the shock-tube diffusion pump. The presence of these same heavy molecules in the background spectrum of the mass spectrometer, also diffusion pumped, supports this implication (see figure 5). The abundance of the 68-71 amu ionic group in the precursor, in comparison to its relative abundance in the shock tube before each run, implies photoionization characteristics that are difference from N_2 or O_2.

3.3b Added Impurities

Small amounts of a specific gas are introduced with the xenon into the test section to study the effect of a particular impurity species. The effects of adding quantities of pure O_2 or N_2 are shown in figure 12. The behavior of the N_2^+ and O_2^+ ions in the case of naturally occurring impurities in Part 3.3a. is the same as in this part if the same partial pressures are initially present in the test section. The maximum spectrometer currents (at the shock front) for the series of runs are shown as a function of the percent abundance of the particular gas species in pure xenon. N_2^+ and O_2^+ ionic

currents are below the mass spectrometer sensitivity for impurity levels below 0.1%. For equal amounts of O_2 and N_2 impurities, the observed abundance of O_2 is higher than for N_2. Currents for both species exhibit a maximum as the impurity level is increased. For impurity levels above about 1%, the xenon ionization levels decrease rapidly, implying a basic change in the radiation chemistry. Figure 13 shows the spectrometer output for the Xe^+ ionic current collected as the shock wave approaches, for three different impurity levels. The precursor ionization currents observed in the double probe and heat transfer gauge traces also decrease if the impurity level exceeds a certain value. It is postulated that for large amounts of foreign gases the shock structure is completely changed; impurity levels above 1% are thus not considered here as applicable in the study of the effect of small amounts of impurities in a typical experimental facility. At low initial pressures, the effect of varying the impurity level is not studied with the spectrometer for Mach numbers less than 18 since at low Mach numbers, it is doubtful that equilibrium is achieved behind the incident shock wave. Certainly, the impurity level has a large effect on the ionization relaxation time, a complex mechanism in itself (see for example, reference 20).

3.3c Impurities in the Driver Section

The role of impurities in the driver gas is also examined. Various amounts of air are left in the driver section before filling with driver gas. Since the hot equilibrium region of the shocked test gas is in contact with the driver gas, it is possible that radiation from the shocked gas is absorbed by the impurities in the driver gas and then re-emitted back through the hot gas (transparent in certain spectral intervals) to the region in front of the shock wave. The radiation source could thus be changed, altering the photoionization mechanisms ahead of the shock. For all impurity levels (up to the level sufficient to change the shock wave velocity) no such effect is noticed in comparison with the pure-driver-gas conditions; both the double probe and the mass spectrometer signals remain unaltered, implying that driver impurities do not influence the precursor phenomena.

3.4 Experiments in Argon

A limited number of experiments were conducted with argon as the test gas. Argon has a higher ionization potential than xenon; therefore, the relative abundance of impurity ions in the argon shock structure may be greater than in xenon. However, the photoionization cross section of argon is lower than that of xenon, which means that the photon mean free path, which is inversely proportional to the cross section is longer (see Appendix E). The

photoionization level in argon should then fall off less rapidly than for xenon.

For initial pressure P_1 = 0.100 torr argon, M_s = 12.2 , and impurity level 0.4%, the mass spectrum shows the presence of only argon ions. Figure 14 shows an indication of the Ar^+ ionic current collected by the mass spectrometer as the shock wave approaches. The maximum sensitivity of the spectrometer must be used at these shock conditions. As with xenon at this low Mach number, no impurity ions are found in the precursor; the impurity ionization levels are probably below the spectrometer sensitivity.

Increasing the Mach number in argon experiments is precluded by the pressure limitations on the spectrometer sampling orifice diaphragm (see Appendix A.6 and B.2); the driver pressures required for higher Mach numbers result in high shock tube final pressures. Replacing the mass spectrometer sampling fixture with a solid shock tube end wall, the effect of higher initial pressures and Mach numbers were studied. Using the double probe as a diagnostic tool, the slopes of the ion density profiles at large distances from the shock wave are found to change in the same manner as with xenon, as the initial pressure is increased (Fig. 9).

IV. THEORETICAL RESULTS

A theoretical model accounting for one-step and multi-step photoionization of xenon and impurities is developed in Appendix E. The analysis is similar to Dobbins' (Ref. 18) for pure argon.

In the present investigation, the existence of ions at large distances upstream of the shock wave are attributed to photoionization caused by the intense radiation from the region downstream of the shock. Using the notation discussed in Appendix E, the conservation equations for ions and excited state atoms produced by radiation ahead of a strong shock wave are

$$-U_s \frac{dN_+}{dx} = R_{oi} N_A + R_{*i} N_* \tag{3.1}$$

$$-U_s \frac{dN_*}{dx} = R_{o*} - R_{*o} N_* \tag{3.2}$$

where U_s = shock velocity

N_* = number density of excited-state atoms

N_+ = number density of ions

N_A = number density of neutral atoms

R = photochemical rates (see figure 15)

x = distance upstream of shock wave in shock-fixed coordinates.

The geometrical configuration is shown in figure 16.

4.1 One-Step Photoionization of Xenon and Impurities

Ignoring contributions due to ionization of excited state atoms, only the first term on the right hand side of equation (3.1) need be considered. Evaluating the rate of one-step photoionization, R_{oi}, the ion number density at a point on the axis of a shock tube a distance η radii upstream of the shocked gas is found (Equation E.6) to be

$$N_+(\eta) = -\frac{4\pi R N_A^{①}}{U_s c^2} \int_{\eta}^{\eta_{max}} d\eta \int_{\nu_{oi}}^{\infty} \nu^2 \, Q_{oi}(\nu) e^{-h\nu/kT^{②}} \cdot \left[\int_1^{\infty} \frac{e^{-\tau_\nu z}}{z^2} dz - \left(1+\eta^{-2}\right)^{-\frac{1}{2}} \int_1^{\infty} \frac{e^{-\tau_\nu (1+\eta^{-2})^{\frac{1}{2}} \psi}}{\psi^2} d\psi \right] d\nu \tag{3.3}$$

where $\eta = \frac{x}{R}$

ν = frequency of radiation

$N_A^{①}$ = number density of neutral atoms in region ①

$\tau_\nu = Q_{oi}(\nu) \, N_A^{①} \eta R$ = spectral optical depth

Q_{oi} = one-step photoionization cross section

$z = \sec\theta = \left(1+\eta^{-2}\right)^{\frac{1}{2}} \psi$

$T^{②}$ = equilibrium temperature in region ②

e,k,h= physical constants

R = shock tube radius

The formulation is general with regard to composition and experimental values are available for the

photoionization cross sections of xenon and many impurities. Substitution of the appropriate values gives an estimate of the ion number density in the precursor for one-step photoionization. Provided the spectral intervals for the photoionization cross section of impurity gas and xenon do not overlap (i.e., all photons are not absorbed by either xenon or impurity), the formulation gives independent precursor ion densities for xenon or for impurities.

The inverse of the optical depth τ_ν is the radiation mean free path, a measure of the distance traveled by a photon of frequency ν before photoionizing a ground state atom. If both the photoionization cross section and the neutral atom number density are large, the radiation is attenuated very rapidly in the cold gas, as shown by the terms in the square brackets in equation (3.3). On the other hand, if either the cross section or the number density is small, photons of sufficient energy for photoionization will propagate further from the wave. Typical values of cross section and number density in the present experiments are given in Table 1. The ground state photoionization cross section for xenon is very large. Hence, if the neutral atom number density (initial pressure P_1 in an experiment) is low the one-step photoionization of xenon is important at large distances from the shock. The photoionization cross sections for

impurity atoms such as oxygen are small and the number densities of such impurities are small in typical experiments. Therefore, it is possible that photon mean free paths are long enough for impurities to become important in precursors.

4.2 Multi-Step Photoionization of Xenon

If the initial pressure is high, one-step photoionization of xenon is negligible at large distances from the wave because of the short radiation mean free path. Solutions of equations (3.1) and (3.2) for ion number densities due to multi-step as well as one-step photoionization must be examined. From Appendix E.3, the photochemical rates R_{oi} , R_{*i} , R_{o*} , R_{*o} are given by equations (E4) , (E17) , (E10) , (E11) , respectively. Long-range transmission of photon energy is important in the wings of the broadened resonance lines in the shocked-gas emission spectrum. The effective "trapping" of resonance radiation in the cold, undistributed gas ahead of a shock wave is also found to be important. The reflection and absorption of radiation at the shock tube walls is necessarily neglected.

For low initial pressures of xenon, one-step photoionization controls the precursor structure. Examination of the relative contribution of single-step and multi-step processes to the total ionization level shows that as the

test pressure increases, ionization of photoexcited atoms becomes the dominate mechanism. Ionization levels due to one-step photoionization decay exponentially with distance, while multi-step ionization levels decrease with some power of the distance from the shock wave. The importance of initial pressure is further noted in that the contribution to ionization due to multi-step processes depends on the square of the number density while single-step photoionization is determined by a linear relation with the number density.

With the appropriate spectral characteristics of xenon and oxygen impurity (Refs. 25-29), thermodynamic properties of high temperature xenon (Ref. 30) and the experimentally determined test-conditions from reference 23, the CITRAN* system is used to obtain a numerical solution to the above equations. Table 1 gives selected values for test conditions and parameters for typical experiments in xenon with oxygen impurity.

Theoretical ion number densities for xenon and oxygen are compared directly with the individual ionic currents collected by the spectrometer in Part V. Re-examination of the theoretical considerations after comparison with experimental results will then yield insight to the validity of the theoretical treatment.

*A Caltech developed on-line computing system using the IBM 360/50 computer. A quadrature integration using Simpson's Rule is utilized.

V. DISCUSSION AND COMPARISON OF EXPERIMENT AND THEORY

5.1 Photoionization at Low and High Initial Pressures

Figure 17 shows the mass spectrometric measurements of xenon and oxygen ions for low initial pressure (P_1 = 0.120 torr) and M_s = 18.5 , where impurity photoionization is found to be significant. The spectrometer calibration constant is used to relate the ion density in the shock tube to the ionic current collected by the spectrometer (see Appendix B.3). For comparison the one-step photoionization calculations (using equation 3.3) are shown for xenon and oxygen at the experimental conditions. At this low initial pressure, the contribution due to multistep photoionization is negligible.

Figure 18 shows the number density of Xe^+ ions as measured by the mass spectrometer at a high initial pressure (P_1 = 0.500 torr) and M_s = 15.2 . Theoretical calculation of ion number density according to one-step photoionization of xenon is seen to decrease to a level several orders of magnitude below the experimentally observed number density. The numerical solution of equation (3.2) , which gives the number density of xenon atoms excited to the first state, is also shown in this figure. Inclusion of this profile for $N_*(\eta)$ in a numerical solution of equation (3.1) results in a contribution to the ionization level, N_+ , which is less in

magnitude than even the one-step photoionization level.

Figure 12 shows the maximum ion density, occurring at the shock front, collected by the spectrometer for various levels of oxygen and nitrogen impurities (see Part 3.3b). For comparison the one-step photoionization levels of oxygen and nitrogen are shown by the dashed lines. At levels above $\sim$ 0.4% for oxygen and $\sim$ 1.2% for nitrogen, the observed number densities depart significantly from the values predicted by theory.

5.2 Precursor Dependence on Shocked Gas Temperature

Figure 8 (Part 3.1) shows the dependence of photoionization on equilibrium temperature behind the shock wave as measured by the double probe. Comparison of theory and experiment at low initial pressures shows that one-step photoionization predominates the precursor, especially close to the shock wave. Examination of the theoretical formulation (equation 3.3) shows that for a fixed pressure the degree of ionization ahead of the shock depends only on the equilibrium temperature behind the wave. Performing the numerical calculations at an initial pressure P_1 = 0.100 torr xenon and at a distance of 5 cm from the shock wave, the ionization level predicted by one-step photoionization is compared in figure 19 with the data obtained by the probe. The two scales have been shifted relative to each other to facilitate a comparison

of slopes.

At the lower temperatures (low Mach numbers) it is doubtful that equilibrium is attained in the shocked gas (even at the given impurity level) and hence the theory, which assumes blackbody radiation at the equilibrium temperature, suggests higher precursor levels of ionization than would be observed. The sharp change in slope of the measured ion current at the lower temperatures substantiates this conclusion.

5.3 Discussion

Correlation between experimental evidence and theoretical understanding of the precursor phenomena is good at low initial pressures, if only small quantities of impurities are present. The small changes in the double probe measurements with variations in the impurity level (Fig. 7) substantiate the spectrometric data. Impurity domination of the precursor at extreme distances from the shock wave is implied by the slopes of both spectrometrically determined and theoretically evaluated ion densities (see figure 17), but the region in which this might occur is below the range of sensitivity of the spectrometer.

At higher pressures, the experimental results show a negligible impurity contribution to the precursor ionization level, due to a different behavior of xenon at large distances from the wave. For the higher initial

pressures, xenon ions are detected at much larger distances from the shock wave than predicted by the one-step ionization theory. The theoretical formulation for multi-step photoionization predicts a high number density of excited-state atoms but ionization from these photoexcited atoms is much lower than the observed values, at the pressures used in the present investigation. Eventual domination by the multi-step ionization process at high pressures is implied by theory (see Part 4.2). In view of the present experimental results, it appears that inadequacies exist in the treatment of multi-step photoionization processes. Experimental implications and theoretical shortcomings in the multi-step photoionization theory will now be discussed.

The experiments indicate the areas which are still not understood theoretically. With the recent work of Schlüter (Ref. 27), the emission spectrum of xenon is fairly well known, but the mechanism of absorption in the cold gas is still not clear. The accuracy of calculations of the edges of the resonance line profiles, which are shown to be important in multi-step photoionization (Appendix E.3), are subject to doubt. The cross sections for excited state photoionization should also be studied further.

Using a somewhat different theoretical approach, Holmes (Ref. 8) found that the main contribution to photo-excitation of ground state atoms comes from radiation in

the wings of the resonance line at frequencies greater than 500 line breadths away from the line center. In this region of resonance radiation on the edge of the line, the blackbody assumption (Appendix E.3) for the emission spectrum and the accuracy of the absorption coefficient are certainly questionable. Experimental studies of this spectral regime are non-existent.

The radiation model as presented, accounts for only the first excited state in the cold gas, although the correction factors (Appendix E.3) for the emission spectra of the hot gas take into account contributions due to recombination of all excited states. Inclusion of the $^1P_1$ excited state of xenon in the cold gas should roughly raise the degree of ionization by a factor of two, still an insignificant amount in view of the present experimental results. It is possible that excitation to levels higher than the first state and subsequent de-excitation to the resonance state (with emission of radiation) may significantly increase the excited atom number density, and consequently, the degree of ionization. Radiation "trapping" (see Appendix E.3) was found to be important by Dobbins (Ref. 18) when he considered photoionization of argon at fairly high initial pressures ($1 \leq P_1 \leq 10$ torr) in a small shock tube ($R = 1.27$ cm). In the present calculations, trapping is important for somewhat lower pressures ($0.050 \leq P_1 \leq 0.5$ torr) due to the larger

(R = 7.62 cm) shock-tube radius; re-emitted radiation has a much longer path length and a higher probability of being absorbed before reaching the wall.

The mass spectrometer results show that for low impurity levels, the impurity photoionization process is uncoupled from the xenon photoionization. The addition of too large a quantity of foreign gas impurities causes a decrease in the magnitude of precursor ionization, suggesting that the shock structure in xenon or the emission characteristics of the radiation source is altered. The presence of radiation from impurities in the hot-gas emission spectrum could have an effect on excited state photoionization of xenon. All components of radiation in the ν_{i*} range are important because of the magnitude of the cross section $Q_* (\nu_{i*})$. Van der Waals line broadening and shifting due to xenon atom collisions with foreign gas atoms may have an effect on theoretical calculations. At some of the higher pressures the effect of neutral impurity atoms could be important on highly-excited states of the primary gas, since highly excited atoms are easily ionized by impurity effects (Ref. 31). The equilibrium volume of shocked gas, i.e., the radiating volume, is increased as the relaxation time is decreased due to the presence of impurities. This would change the emission characteristics of the radiating gas.

In the theoretical treatment of the radiation mechanism, the non-equilibrium region between the frozen shock front and the equilibrium zone is excluded from consideration. Biberman and Yakubov (Ref. 32) discuss propagation of resonance radiation through this region; further study of radiation in this important region is in order.

The effect of the reflected radiation from the shock tube walls could be of major importance. Wall reflectivity would certainly increase the level of ionization ahead of the shock wave because of increased photon flux from the shocked gas. The region far from the shock wave is distinguished by the large discrepancies between the experimental and theoretical results. The effect of reflection would be much larger at distances far from the shock wave since the theoretical solid angle subtended (at a point on the shock tube axis) by the hot gas is much smaller at these distances than when the radiating gas is closer. At points close to the shock wave, more of the radiation from the shocked gas is included in the geometry and hence the additional reflected radiation would be proportionally less. Thus, more photons propagate further down the shock tube than the geometrical attenuation factor in the theory suggests.

It should be noted that the reflectivity function is extremely important in the photoionization of photoexcited

atoms, since both the photoexcitation and photoionization rates would be multiplied by the reflection property. Also, photon absorption at the wall is greater for ultraviolet radiation with sufficient energy for one-step photoionization than for longer wave-length radiation, so the reflectivity for longer wave-length is higher, since the sum of absorption and reflection coefficients is constant. Reflection of this radiation with sufficient energy to photoexcite and then to photoionize neutral atoms should be very important in the multi-step photoionization process. Study of absorption and reflection coefficients for solid surfaces in the ultraviolet spectrum presents a formidable problem; hence, the effect is not considered in the theoretical formulation (see Appendix E.2).

The present investigation is primarily concerned with determination of the radiation-induced properties of the leading section of the shock wave structure. For a complete understanding of the structure of strong shock waves, these results must be coupled through the non-equilibrium zone with the equilibrium conditions in the trailing section of the shock wave. For example, pre-ionization in the precursor region greatly influences the ionization relaxation to equilibrium by increasing the availability of free electrons for electron-atom ionization collisions. Theoretical attempts at relating these regions are given in references 33 and 34.

VI. CONCLUSIONS

Comparison between predicted values of impurity ionization and experimental evidence implies that at least for small quantities, the role of impurities in the precursor phenomena is understood and can be estimated fairly accurately. For small impurity levels, the impurity ionization can be uncoupled from photoionization in pure xenon, and this region of the total shock structure in xenon may be studied. Theoretical calculations of one-step photoionization of xenon at low initial pressures ($P_1 \sim 0.100$ torr) afford good agreement with observed number densities. The dependence on temperature at short distances from the shock conforms to the radiation model. At these low pressures, impurity ionization is of the same order of magnitude as xenon ionization, due to the longer radiation mean free paths for impurity atoms. At higher pressures ($P_1 \sim 0.500$ torr), difficulties in the theoretical interpretation of the observed magnitudes of the precursors cannot be attributed to one-step xenon or impurity photoionization. The general agreement of the one-step mechanism for lower pressures and disagreement at high pressures implies that the important ionization mechanism for higher pressures is multi-step photoionization. The theoretical treatment of multi-step photoionization processes proves to be inadequate and further work on ionization from an excited state is

in order. Theoretical treatment of photoexcitation and ionization from states above the first excited state have yet to be made. The accuracy of the cold gas absorption line broadening mechanisms controlling the far wings should be subjected to experimental verification.

The very important dependence on the shock tube wall reflectivity, at the wavelengths suitable for excited state-ionized state transitions, indicate that experimental study of this subject should be the next step in the study of precursors.

APPENDIX A

THE GALCIT 6" SHOCK TUBE

The GALCIT 6" shock tube was designed* as an intermediate-sized facility for the production of strong shock waves under very reproducible conditions (an essential prerequisite in this study). It is well suited for studying various reaction rate phenomena, highly ionized plasmas, and radiation effects. The simplicity and repeatability of a cold gas driver was found extremely beneficial, and great attention was paid to achieving an accurate control over the impurity level in the test section. In the following discussion the basic dimensions, vacuum characteristics, and instrumentation pertinent to the present investigation are described.

A.1 Description of the Basic Shock Tube System

A schematic of the shock tube and associated equipment is shown in figure 1 (see also figure 2). The tube consists of a cold-gas driver section, a diaphragm-transition section and a 36' long driven (test) section. The mass spectrometer is mounted on the end wall (mechanically isolated from the shock tube), and a pressure-relief tank is connected to the shock tube at two ports near the end wall.

*Complete and detailed descriptions of the shock tube facility are found in references 22 and 23.

The driver section is a 6' length of 6.520" I.D., type 321 stainless steel, seamless tubing with a wall thickness of 0.5". The driver gas inlet, driver pressure-gauge line, driver vacuum-pump line, and the external exhaust line are all mounted on the driver section end wall. A mechanical vacuum pump evacuates the driver before each run.

A unique hydraulic system supplied the force necessary to clamp the diaphragm in place in the diaphragm-transition section. A set of crossed knife blades mounted across the transition section uniformly cuts the diaphragm as it bulges under pressure (Ref. 35). Variation of diaphragm material (usually aluminum sheet), diaphragm thickness, curvature of the knife blades, and different mixtures of the driver gases (hydrogen, helium, and nitrogen) provide a continuous range of shock Mach numbers. The bursting pressures for various diaphragm materials and thicknesses are repeatable to within 3 psia or less, resulting in very good reproducibility of shock conditions. Squaring plates downstream of the diaphragm section provide a flat edge for the diaphragm metal to bend on, eliminating tearing and loss of the diaphragm petals after rupture.

Three 12' lengths of type 321 stainless steel seamless tubing with a nominal wall thickness of 0.5" form the driven test section. The internal surface of this section is honed to a finish of 10 to 20 microns. Observation of

strong reflection of visible light in the test section suggests that radiation may be important in the present investigation; further reference to this possibility is made in Appendix E. The internal diameter of the tube is 6.021 ± 0.002 inches with a maximum step height at any joint between sections of less than 0.002". Also, all instrumentation in the tube was machined to the contour of the tube, minimizing any flow disturbances.

Instrumentation ports are located at various positions in the shock tube. Each port consists of one inch (0.935") diameter access hole with a 2-1/8" diameter flat (for O-ring seals) on the outer surface of the tube.

The tube was designed to have good vacuum characteristics. Neoprene O-rings are employed in all tube joints, ports, and valves, and the plumbing is soldered. The stainless steel wall material and the honed internal surface enhance the vacuum performance.

The vacuum system consists of three pumps. Two mechanical vacuum pumps (a Kinney, Model KC 46 and a Welch, Model 1397B) evacuate the driver and test sections to a pressure of a few microns. In addition, the Welch pump serves as the fore pump for a six-inch oil diffusion pump. A liquid-nitrogen cold trap is located between the diffusion pump and the shock tube. The pumping line ports are positioned in the transition section to minimize flow disturbance in the test section.

For the present investigation research grade Linde xenon (50 parts per million impurity level) is used, and for the few experiments in argon, Linde argon (400 parts per million impurity level) is used. Type 555 (Tektronix) dual beam oscilloscopes and Type L fast-rise pre-amplifiers are utilized to obtain all data, unless specific note is made otherwise. A Beckman, model 7370, tenth-microsecond time interval-counter is used to set all oscilloscope delays. Polaroid film furnishes permanent records of the oscillograms.

A.2 Operating Conditions and Limitations

For the present study, an accurate control of the impurity level is imperative. This is accomplished by pumping the test section to a pressure far below that required to give the desired impurity level and then allowing the tube to leak "impurities" and to outgas up to the required pressure. Alternatively, a particular species of impurity is introduced following the initial evacuation.

With the present pumping system, the driven section can be evacuated to a pressure of 0.03×10^{-3} torr in three-quarters of an hour, and after this time, the combined leak and out-gassing rate is less than 3.0×10^{-3} torr per hour. An ultimate pressure of 0.007×10^{-3} torr can be attained after four hours of diffusion pumping with a corresponding initial leak and out-gassing rate of 1.7×10^{-3}

torr per hour. Use of solenoid valves allows remote control of the shock-tube system, so the shock tube may be fired a few seconds after the test gas is introduced, minimizing additional out-gassing and leakage.

The shock tube is capable of withstanding pressures far in excess of the allowable maximum operating pressure at the entrance to the mass spectrometer, so the mass spectrometer imposes the limiting condition on initial pressure, driver pressure, and Mach number. A typical value of driver pressure for the xenon experiments is 120 psia hydrogen.

Experimental determinations of operating parameters (e.g., relaxation time) for the 6" shock tube are presented in reference 23. For a representative condition (initial pressure of 0.120 torr xenon, and $M_s = 18.5$), the shock tube produces a slug of test gas that is approximately 15 cm in length on reaching the end wall of the shock tube with an ionizational relaxation region about 3 cm long. The equilibrium degree of ionization behind the incident wave is 0.36, and the equilibrium temperature is 9800^{o}K.

A.3 Determination of Shock Wave Velocity and Position

Accurate determination of the shock Mach number and the precise moment at which the shock reflects from the entrance of the mass spectrometer is critical in this investigation, since mass spectrometric data must be

compared for many experiments (see Section 2.2). The responses of two flush-mounted platinum thin-film heat-transfer gauges and the electrical response of a piezoelectric crystal are used to measure the incident shock wave velocity and to trigger the other electronic apparatus. The conventional method of measuring shock velocity by using a microsecond counter to measure the time interval for shock passage over the distance (50 cm) separating the two sidewall gauges is unsatisfactory due to the effect of precursor ionization on the electrical response of the gauges (see, for example, reference 36). In extreme cases it is very difficult to even identify the shock wave on an oscillogram of the side-wall gauge output since the precursor signal is often larger than that due to the temperature change induced by the shock front.

An electrically-shielded piezoelectric crystal (Clevite PZT-5) 0.25" long, 0.0625" wide, and 0.040" thick is mechanically isolated from the shock tube with Dow-Corning RTV 601 silicone rubber and located in an instrumentation port diametrically opposed to the side-wall gauge closest to the end wall (see figure 20). In this manner the precise location of the shock wave is determined from the response of the crystal to the pressure discontinuity at the front of the shock wave.

One beam of an oscilloscope records the output of the upstream thin-film gauge, the beam being triggered by the

precursor signal ahead of the shock wave. A second and third beam are delayed from this trigger and are used to display the output of the second thin-film gauge and the piezoelectric gauge, both located 50 cm downstream from the first thin-film gauge. Examination of the piezoelectric gauge signal determines the shock-wave location in the side-wall gauge oscillogram and fixes the spatial position of the shock relative to the end wall of the shock tube (i.e., the entrance to the mass spectrometer). A comparison of typical signals from the piezoelectric crystal and the thin-film gauge is shown in figure 21.

Using the piezoelectric trace, the shock wave can be located on the two similar thin film gauge traces, and the time interval for shock passage can be determined from the oscillograms. An estimate of the error in determining the shock wave Mach number in this manner is $\pm$ 1%.

A.4 Measurement of Initial Pressure and Impurity Level

Accurate knowledge of the initial partial pressure of both the primary gas and impurity gas is of major importance. One of two calibrated volumes either 1/200 or 1/30 of the volume of the shock-tube test section is used to fill the shock tube with the test gas; the calibrated volume is filled to a pressure proportionally higher than the required final pressure by the inverse of the volume ratio. The higher pressure is measured on a 0-50 torr, bellows-type

Wallace and Tiernan gauge. The control volume ratios are calibrated in air with a McLeod pressure gauge (isolated by a cold trap). A Hastings-Raydist thermocouple vacuum gauge (0-1 torr) and a Consolidated Vacuum Corporation model GPH - 100A cold-cathode ionization gauge (10^{-6} to 10^{-3} torr) are used to measure pressure in the range down to the ultimate pressure of the vacuum system.

For controlling the impurity levels, two methods are used. The first is to inject a pure species of foreign gas by filling the control volume to the required pressure (i.e., 200 times the resultant partial pressure in the shock tube) of impurity gas. The primary gas is then introduced into the control volume and adequate time is allowed for thorough mixing before injection into the test section. Several gas cylinders and valves are located on the control volume system for conveniently changing the desired species of gas. To facilitate determining small pressures in different gases in the control volume, the McLeod gauge is employed.

For "naturally-occurring" impurities (i.e., foreign gas introduced by outgassing and shock-tube leaks), the shock-tube test section and pressure measurement system is pumped to a high vacuum and closed off. After an interval of time the shock tube fills with impurities to a predetermined pressure. The primary gas is then introduced in the conventional manner.

A.5 Natural Impurities Present in the 6" Shock Tube

As discussed in the preceeding section, the "naturally-occurring" impurity level for each run is calculated by finding the leak and out-gassing rate of the shock tube and observing the time elapsed between closing the diffusion pump and bursting the shock tube diaphragm. By connecting the shock-tube test section directly to the gas inlet of the spectrometer ion source (see Appendix B.1) and closing off the diffusion pump so the shock tube will leak and out-gas, the impurity gases present in the test section enter the ion source and are analyzed by the mass spectrometer. The mass spectrum is scanned by monitoring (with an X-Y recorder) the ionic current as a function of either the spectrometer magnetic field strength of accelerating potential. A typical mass spectrum schematic is shown in figure 5.

The relative abundance of impurities present in the shock tube depends on which gas previously occupied the test section, the vacuum level to which the test section is pumped, the length of time the tube had previously been exposed to atmospheric pressure, variation in atmospheric humidity, and the pressure in the shock tube during the mass spectrum scan. In general, the predominant impurities are (in order of decreasing abundance) H_2, H_2O, O_2, and several groups of hydrocarbons. The level of water vapor

shows the greatest variation with initial conditions, sometimes becoming the predominant impurity. For longer time intervals between closing off the test section and sampling impurities with the spectrometer, the contributions due to molecular oxygen and nitrogen increases greatly (leakage), while the hydrocarbon level remains fairly constant, as expected. The magnitudes of the ionic currents due to the residual gases in the mass spectrometer itself prevented determination of the extremely small levels of impurities present in the test gases used in the shock tube. The spectrometer background spectrum is also shown in figure 5.

A.6 Pressure Relief System for the 6" Shock Tube

As will be explained in Appendix D (Typical Experimental Procedure), a movable source of ions is used to set the mass spectrometer for a specific mass peak before each run. The source slides out of the system, exposing the inside of the shock tube to the sampling orifices in the spectrometer. After the shock wave hits the end wall (sampling holes) the sliding source moves back into place, closing off the spectrometer from the shock tube. The surfaces of the electron multiplier are very sensitive to high gas pressures, and this sensitivity requires that the source valve close as rapidly as possible to isolate the high final pressure in the shock tube from the spectrometer.

The tolerances of the sliding source are critical. The valve must be vacuum tight yet must slide easily.

The final pressure after an experiment in the 6" shock tube is often above one atmosphere. If this pressure remains high then the sliding valve binds in its tracks necessitating a method of relieving the pressure forces.

A large pressure relief tank (14.2 ft^3) was fabricated from spare sections of the 17" shock tube. This dump tank is isolated from the shock tube by an expendable, thin plastic diaphragm. A diaphragm material is used such that a pressure slightly less than one atmosphere is sufficient for rupture. Outgassing or leakage of the thin diaphragm is found to be negligible even at the extreme vacuum of the shock tube. Operating the mass spectrometer with and without the diaphragm system has no noticeable effect on the ion currents observed. Vibrational movement of the shock tube during a run requires that metal bellows tubing be used to isolate the tube from the tank system. A mechanical vacuum pump (exhausting through the roof) evacuates the tank before each run and expels the hydrogen remaining after each experiment.

The mounting location of the mass spectrometer system at the shock tube end wall requires that the dump tank connecting lines be mounted at two diametrically opposite instrumentation ports 10 cm from the end wall. Two ports are sufficient to equalize the pressure in less than a

second (see figures 3 and 4). Since the tube forming the entrance to the spectrometer sampling region (see Appendix B.1) extends past these ports, the supersonic nature of the flow behind the shock wave prevents any disturbances created by the ports from propagating back to the entrance of the spectrometer.

APPENDIX B

THE MASS SPECTROMETER

The spectrometer in the present investigation is a modification of the Nier (1947) type mass spectrometer (Ref. 20). In the following discussion, the physical characteristics and operational features of the instrument will be given, along with details relevant to the present application.

In principle, the spectrometer is simple (see figure 4). The spectrometer is located at the end wall of the shock tube, sampling the region in front of an approaching shock wave. Ions produced by photoionization are drawn by an applied electric field into the spectrometer and electrically accelerated to a high velocity in a collimated beam. The beam is deflected, depending on the mass to charge ratio, when it passes through the field of a large magnet. Ions of a particular mass then impinge upon the exposed cathode of an electron multiplier. The measured multiplier current is then directly related to the abundance of the particular ionic species at the end wall of the shock tube. An integral ion source is used to set the particular mass peak before each run.

High mass resolution and extremely fast time-response are obtained by observing the time history for only one mass peak during each run. On the other hand, several runs

are required to obtain the complete spectrum, making duplication of experimental conditions very important.

B.1 Physical Characteristics of the Spectrometer

To mechanically isolate the spectrometer from the shock tube, the spectrometer is supported from the floor and connected to the shock tube by a flexible bellows (Fig. 3). The actual end wall, on which are mounted the sampling orifices, is inside the spectrometer structure. To prevent flow disturbances, e.g., from the pressure relief system (see Appendix A.6) or the shock tube end wall, a "cookie cutter" (3" diameter stainless steel cylinder, sharpened at the open end) extends upstream into the shock tube and cuts out the center section of the approaching shock wave. This section then propagates undisturbed to the spectrometer entrance, a thin diaphragm containing several sampling orifices.

Ideal sampling occurs when the composition of the sampled gas does not change during the sampling process, i.e., when the reactions in the sample are frozen from the region of sampling to eventual ionic current collection. This can only be accomplished by rapidly expanding the sampled gas to a low density without allowing collisions to take place (e.g., by free-molecular effusion from an orifice). A criterion that must be met for free molecular effusion (see reference 37) is that the Knudsen number

$Kn > 1$, where $Kn = \lambda/d$ (λ = mean free path at the sonic point in an orifice, d = diameter of the orifice). Therefore, the orifice diameter should be very small, yet the flux (ion current) through the hole must be as large as possible to ensure that signals be detectable. Therefore, several small diameter orifices are used (up to thirty 0.015 cm diameter holes in a double row aligned with the first slit of the spectrometer). Under the test conditions for the present investigation, the criterion is met reasonably well. A typical test condition shows that the mean free path for an initial pressure of 0.100 torr xenon is $\lambda = 0.053$ cm and the orifice diameter $d = 0.015$ cm, so that $Kn \sim 3.5$.

The limit on the maximum number of orifices exposed to the shock tube for a particular test condition (i.e., the largest ionic flux) is such that ions inside the spectrometer will not undergo collisions before being collected at the cathode of the electron multiplier. This requires that the pressure inside the mass spectrometer during an experiment must be less than 7×10^{-5} torr. A 4" oil diffusion pump (ultimate pressure $\sim 10^{-6}$ torr) isolated from the spectrometer by a liquid nitrogen cold trap, is connected directly to the spectrometer tube. Typically, the pumping system is sufficient to maintain the required pressure in the spectrometer when the shock tube containing

xenon at 0.100 torr is exposed to the spectrometer through 12 sampling orifices.

A sliding rectangular block (the "spectrometer valve") contains both the sampling orifices and the ion source used to set a particular mass peak just before a run (a detailed description is given in reference 20). In one position, the ion source is exposed to the spectrometer and the shock tube is closed off. In the other position, the mass spectrometer draw out slit is aligned through the sampling orifices, with the center of the inside of the shock tube. The spectrometer valve is pneumatically actuated. After each run, a signal from an oscilloscope turns off the spectrometer voltage and starts the valve closing.

The ion source is a small electron beam device. A tungsten filament emits electrons which are accelerated by a potential difference and are used to ionize any neutral atoms introduced into the source chamber. A mixture of gases may be analyzed by allowing a small amount of gas to flow into the ion source. Variation of an independent parameter such as the magnetic field strength or the accelerating potential changes the particular mass peak being observed (basic relation is $m/e \sim B^2/V$ where m/e = mass to charge ratio, B = magnetic field strength, V = accelerating potential). Inputting the electron multiplier current and the varying parameter to the X and Y inputs of an X-Y recorder provides a mass spectrum of

the particular foreign gas. In this manner, for example, the "naturally-occurring" impurities in the shock tube are determined.

Ions from either this source or from the sampling orifices (when exposed to the shock tube) are attracted by the draw out plates (-22 to -135 volts) into the region of the accelerating slits. There, the ions are accelerated to a potential of from -1000 to -2000 volts and the collimated beam passes into the magnetic field (100 to 4500 gauss) produced by passing current through two large magnet coils. Current for the coils is supplied by two fast rise-time regulated power supplies (PMC Uni-88). The tubular envelope surrounding the beam is made of nonmagnetic stainless steel and is at the same potential as the accelerator slits.

The analyzed and focused ion beam then impinges on the resolving slit (the width of which determines the resolution of the instrument), and collected on the first dynode of the electron-multiplier. By changing slit dimensions, several adjacent mass peaks may be examined collectively, or individual mass peaks may be considered separately. The mass resolving power is adjustable from 1 in 10 to 1 in 200. A typical mass spectrum obtained by monitoring the ion current from the source as a function of a variation in the magnitude of the magnetic field (constant acceleration potential) is shown in figure 5.

Likewise, holding the magnetic field strength constant and varying the potential would produce a similar representation.

The ten-stage electron multiplier (Dumont SPM 18-01-401) is operated at the same potential as the accelerator (voltage supplied by a regulated power supply, John Fluke Model 412 B). It has a current gain of about 1000 and its anode is connected to the input of a fast rise-time operational amplifier (Philbrick P25AH) used as a current-to-voltage converter. Using this circuit the output is then monitored on a Tektronix type L preamplifier and a type 555 oscilloscope.

The time response of the detector system is one microsecond, making it a valuable tool in shock-tube applications. The time of flight in the spectrometer is from 1 to 7 microseconds depending on the acceleration potential and the ion mass. The stability of the power supplies for the accelerator and magnet is such that once having been set on a particular mass peak there is no perceptible drift from that peak for as long as half an hour.

B.2 Operating Conditions and Limitations of the Mass Spectrometer

The shock tube initial pressure is limited to a magnitude such that when the mass spectrometer is connected to the shock tube through the sampling orifices,

its pressure must be less than 7×10^{-5} torr (collisionless flow in the spectrometer). The total area of the sampling orifices must ensure observable ionic currents in the spectrometer; the higher the initial pressure, the fewer the number of sampling holes which may be exposed, and correspondingly, the smaller the currents collected. In the present investigation the highest shock-tube pressure feasible under this criteria is 0.500 torr, with two 0.015 cm holes forming the sampling openings into the spectrometer. This is a practical limit from another point of view. At higher test pressures (i.e., $Kn \ll 1$), the sampling process becomes more complex. The free molecular flow requirement is no longer satisfied, and a supersonic free jet is formed in the spectrometer, causing an extremely complicated interaction with the accelerator electrodes.

In addition to the initial pressure, a limit also exists on the Mach number. The thin diaphragm containing the sampling holes is dynamically subjected to the high pressures behind the reflected shock wave in the shock tube. To prevent rupture, combinations of Mach number and initial pressure are used so that the pressure in the reflected region is much less than the value (40 psia) to which the spectrometer diaphragm has been statically tested. The limiting condition is an initial pressure of 0.500 torr at a Mach number of 16.

Due to the strong electric fields in the drawout-accelerator arrangement, only about 0.01 percent of the ions drawn into the spectrometer pass entirely through the ion optical system to be collected by the electron-multiplier. The existing configuration is operational for ion densities (in the shock tube test section) of from 10^9 ions/cm^3 to 10^{12} ions/cm^3. The signal-to-noise ratio of the electronic system determines the lower limit, and mutual repulsion in the ion beam limits the maximum ion density sampled (Ref. 38).

Assuming the shock wave velocity remains constant in the distance from the piezoelectric gauge to the mass spectrometer (34.9 cm) the arrival of the shock wave at the mass spectrometer sampling orifice can be determined. Observation of the ion current from the mass spectrometer at shock arrival verifies the expected time interval. At the calculated arrival time, a step-function increase in current is observed on the spectrometer current output (Fig. 22), probably attributable to a short-circuiting effect on the draw-out or accelerator electrodes by the highly ionized plasma behind the shock wave. To prevent subjecting the electron multiplier to large bursts of ionic current at this time, a pulse generator is capacitively coupled to the draw-out circuit to pulse the draw-out electrodes positively (+100 volts) to repel ions away from the sampling holes. The pulse is timed to

start at shock reflection and remain on until the high voltage on the electron multiplier is automatically switched off a few milliseconds later.

B.3 Mass Spectrometer Calibration

The mass spectrometer is basically a qualitative instrument, but under the present conditions, a semi-empirical calibration may be determined. The calibration constant for the spectrometer is defined as the ratio of the measured spectrometer current to the ion number density in the gas inside the shock tube test section. The ions must be drawn into the spectrometer sampling region, accelerated and collimated by the various electrodes, analyzed by the magnetic field and then focused and collected by the electron multiplier.

For the conditions of the present investigation (Kn > 1) free molecular flow may be assumed around the region of the sampling orifices, and the ionic flux (current) drawn into the sampling orifices may be expressed as

$$\frac{i}{N_+} = \frac{n\pi D^2 e}{16}\left(\frac{8kT_+}{\pi m_+}\right)^{\frac{1}{2}} \quad \left\{\text{amps/ion/cm}^3\right\} \qquad \text{(B1)}$$

where i = ion current

D = diameter of sampling hole = 0.015 cm

n = number of sampling holes exposed

e = electron charge

T_+ = ion temperature (assumed equal to neutral atom temperature) = 300° K

m_+ = mass of ion

N_+ = ion number density

k = Boltzmann constant.

The efficiency of the drawout-accelerator configuration is found by measuring the ratio of current collected by the electron multiplier to that collected by the drawout plates and accelerator slits. This factor is experimentally found to be 2.5×10^{-4}.

The current gain of the 10-stage electron multiplier is a function of the ionic species being collected and the potential of the accelerator (beam velocity) and multiplier dynodes. In general the gain can be expressed as $f(m_+, V) \times 10^3$, and the total calibration constant (collecting xenon ions, for example) giving the relation between current output from the spectrometer and ion density in the shock tube is given by

$$K = \frac{i}{N_+} \cdot (2.5 \times 10^{-4}) \cdot [f(m_+, V) \times 10^3] \qquad (B2)$$

$$= 3.9 \times 10^{-20} \cdot n \cdot f(m_+, V) \quad \{\text{amps/ion/cm}^3\}$$

where $f(m_+, V)$ is determined experimentally and $0.3 < f < 1.5$ in the present application.

APPENDIX C

THE LANGMUIR DOUBLE PROBE

Since the mass spectrometer is basically a qualitative instrument and its calibration constant (relating the collected ion current to the number density in the shock tube) is only a rough approximation, a Langmuir probe is used to provide an independent measurement of the number density. Observation of the total ion current collected during each run assures repeatability of precursor ionization levels while the individual currents are collected by the spectrometer.

A double probe system that essentially "floats" at the plasma potential is used for minimal interaction with the precursor plasma. Under particular operating conditions, an interesting resonance phenomenon is observed, which leads to a further independent determination of number density. This effect is described in detail.

C.1 The Langmuir Double Probe As a Diagnostic Tool

The simple electrostatic probe is attractive as a charged particle measuring device in a shock tube since it has spatial resolution characteristic of its dimensions, and under certain circumstances, the collected current provides a measurement of the ion number density. The double probe technique was first proposed by Johnson and Malter (Ref. 39). The method makes use of two collecting

probes biased by a differential voltage (see figure 6). The entire system is electrically floating and follows the plasma potential. At any instant the total current of positive ions and electrons flowing to the system from the plasma in the shock tube must be zero.

In the present investigation, the probes are biased at a potential large enough to ensure ion saturated currents. Assuming that the ionic current falling on the probe is characteristic of the random thermal motion in the gas ahead of the shock wave, (a reasonable assumption, in light of the low density and temperature) the ion number density is obtained through the relation (free molecular flow)

$$N_+ = \frac{4}{Ae}\left(\frac{\pi m_+}{8kT_+}\right)^{\frac{1}{2}} i_p \,, \qquad (C1)$$

where A is the probe surface area, e is the electronic charge, m_+ is the ionic mass (The predominant ion collected is determined by the spectrometer), T_+ is the ion temperature (approximately the neutral atom temperature), k is Boltzmann's constant, and i_p is the current in the negative probe. The requirements for the free molecular approximation are that the mean free path in the surrounding gas is such that no collisions occur in the electrostatic "sheath" (characteristic dimension of a Debye length) surrounding each probe, and that the probe

radius is smaller than a mean free path. In the present investigation, initial pressures are such that the latter criterion is only marginally satisfied.* This method of obtaining the ion number density with the free molecular flow model (even at conditions where the mean free path is smaller than the present application) has been recently supported by microwave cavity calibration experiments (Ref. 40).

C.2 Description of the Probe and its Application

The probe system consists of two 0.021" diameter tungsten wires 0.512" in length, mounted 0.1" apart in a metal-ceramic plug. The plug assembly, contained in a thin film gauge canister, is mounted in one of the various instrumentation ports of the shock tube, the two wires lying in a plane perpendicular to the shock tube axis (see figure 6). A battery and shunting capacitor supplies a constant emf across the two wires. A Tektronix type D differential pre-amplifier in conjunction with a type 555 oscilloscope monitors the potential change across a 100-ohm series resistor, yielding the probe ionic current as a function of time as the shock wave approaches. Several

---

* For initial pressure P_1 = 0.100 torr xenon, mean free path = 0.5 mm; for electron number density $N_e = 10^{10}$ cm^{-3}, Debye length = 0.01 mm; and probe radius = 0.25 mm.

experiments are conducted to determine the value of bias voltage necessary to ensure ion-saturated currents for each precursor condition. A potential of -15 volts is found sufficient for the highest precursor levels encountered in the present investigation. The differential voltage across the probes is monitored for the largest precursor currents collected and is found to remain constant.

Photoemission from the probe surface is found to be negligible by altering the probe orientation with respect to the radiation region of the approaching shock wave (e.g., aligning the probe axis with the shock tube axis, exposing only the probe ends to the radiating gas), changing the probe surface area exposed to direct radiation. To ensure that the electric field between the two probes does not alter the responses, another mounting system is constructed in which the two probes are separated by 0.75". Under the same initial conditions the current profiles are very nearly the same.

To assess the effects of the cookie cutter entrance to the mass spectrometer, some experiments are run with the double probe axes aligned with the shock tube axis. In these runs, the probe system is mounted in the end wall (in place of the spectrometer), and experiments are run first without the cookie cutter and then with the probes inside the cookie cutter and the current traces are

compared. In general, the currents using the cookie cutter are smaller than without the cookie cutter, due to the reduced radiating volume of hot gas behind the shock. For all graphical comparisons of probe and spectrometer currents, the probe data are obtained with the double probe inside the cookie cutter in the same position as the sampling orifices.

C.3 Measurements of Number Density with a Mexican Radio Station

For certain conditions existing during the shock tube experiments, a small localized perturbation is observed on the double probe precursor signal (see Figs. 23, 24). Examination of similar experiments in both the 6" shock tube and the GALCIT 17" shock tube discloses the phenomenon occurring on the signal from the electrostatically-exposed thin-film side wall gauges used to monitor shock position.* Under particular circumstances (i.e., low pressure, P_1 = 0.120 torr xenon, M_s = 18.5, spectrometer draw-out potential = 44 volts), the mass spectrometer traces show the same "bump". During high Mach number experiments using an electron beam apparatus in the 17" shock tube, the interaction of the electron beam with the precursor yields a perturbed signal similar to the double probe

*Compare, for example, GALCIT 6" shock tube run 632 (April 18, 1968) with GALCIT 17" shock tube run 1903 (April 5, 1966). [These unpublished records are available in the laboratory log books of the respective facilities.]

signal in the 6" shock tube.* As conditions are varied, (e.g., initial pressure and Mach number), the perturbation is observed to shift with respect to the shock wave location, but remains at approximately the same absolute magnitude of probe ion current (i.e., ion number density).

It is well known that the current from a high-frequency driven Langmuir probe immersed in a plasma exhibits a sharp peak at the frequency corresponding to the electron plasma frequency of the plasma (see for example, reference 41). Since the electron plasma frequency is directly related to the electron number density, detection of electron resonance in a plasma yields a determination of the number density.

Recently, resonance behavior has been observed near the ion plasma frequency in gas plasmas produced by electrical discharges (Refs. 42, 43). Because of the much lower frequencies involved, application of an ion resonance probe would be very attractive in shock tube flows.

---

*GALCIT 17" shock tube runs 2476-2487, (May 4 - May 7, 1967).

The electron resonance probe technique is schematically represented as

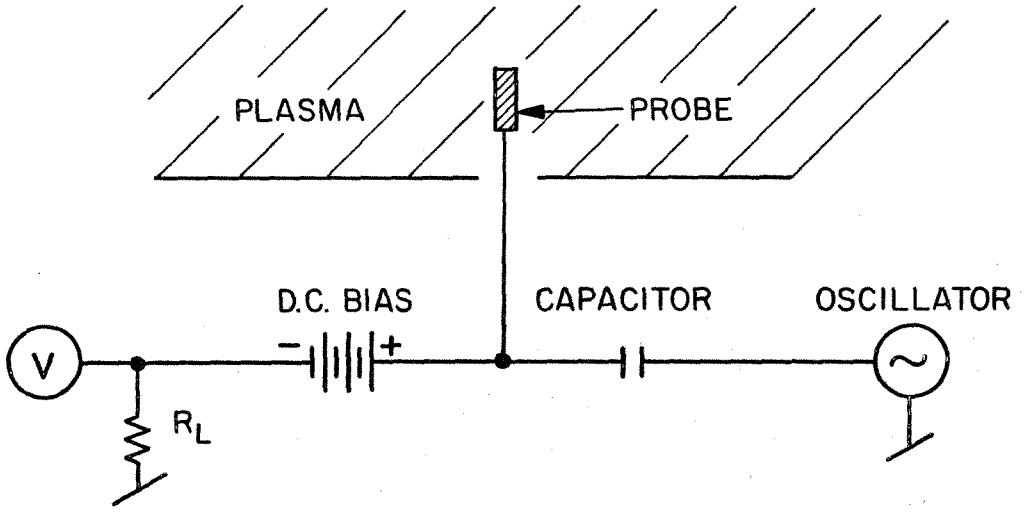

The steady state plasma behaves inductively and the sheath region close to the probe capacitively. When a high frequency signal is imposed on the probe by an oscillator, a series resonance occurs in the plasma at the electron plasma frequency. At resonance, the high frequency electric field occurring near the probe in the plasma causes an increased rectified current to flow into the probe circuit. The electron plasma frequency is related to the electron number density by

$$\omega_e^2 = \frac{e^2 N_-}{e_o m_-} \qquad \text{(C2)}$$

where ω_e = electron plasma frequency

e = electronic charge

N_- = electron number density

ϵ_o = permittivity of free space

m_e = mass of electron.

For an ion resonance probe the probe is biased negatively and the ion plasma frequency is given by

$$\omega_+^2 = \frac{e^2 N_+}{\epsilon_o m_+} \quad . \tag{C3}$$

Two modes of operation are suggested. An imposed frequency scan with an electronic oscillator in a steady state plasma (fixed ion number density) would result in a peak in the ion current at the frequency corresponding to the correct number density. Alternatively, for a constant imposed frequency, a temporal variation in ion number density would result in a change in the current at the density corresponding to the related ionic frequency. This approaches the conditions in the shock tube. The double probe (see figure 6) is subjected to an increasing ion number density in the precursor as the shock wave approaches. If a constant external forcing frequency were imposed (coupled to the probe circuit or plasma) the probe might resonate when a particular number density occurred near the probe. Observation of the collected current

should allow determination of the ion number density at that instant, thus inferring the correct probe current-number density calibration relation.

It was found that the ground reference (see figure 25) for the electrical systems in both shock tube facilities oscillates (frequency ~ MHz) with a magnitude of about 100 millivolts (variable from day to day). Most of the noise is attributed to a local radio transmitter (mainly playing Spanish music). A brief prearranged interruption of transmission power at 3 AM one morning resulted in the disappearance of approximately three-fourths of the noise magnitude and predominant frequency.

It is postulated that this high frequency signal imposed on the shock tube and associated circuitry gives rise to the required forcing frequency for the ion resonance effect. As the ion number density increases due to the precursor ahead of a strong shock wave, the number density rapidly passes through the valve corresponding to that frequency resonance, resulting in a small change in the current collection by the probe. Changing the precursor level corresponding to this particular number density with respect to its distance from the shock wave (e.g., changing the shock Mach number) should result in a relative shift in the observed "bump". This is experimentally realized.

That the phenomena is not due to a potential or induced effect is verified by covering the double probe with insulating sleeves. The "bump" and the collected current disappear, implying the phenomena is associated with the physical collection of charged particles on the probe. At initial test pressures above 0.300 torr the disturbance becomes negligible, suggesting collisional damping in the probe sheath region. Also, a conventional Langmuir probe (i.e., one probe in series with a battery) is biased negatively and positively at different voltages. The peak is also observed for this probe, and it becomes sharper at lower potentials and becomes less pronounced at higher potentials.

Examination of the perturbation with a Tektronix type 10A1 differential amplifier (bandwith 40 MHz) and a type 647A oscilloscope shows high frequency oscillations of the current in the region of the "bump" (see figures 24, 26). Actually, the high frequency noise on the electrical ground sometimes appears modulated. Modulationed envelopes are also exhibited in the fast rise-time records of the probe current. Higher frequency components of lesser magnitude are also observed on the primary frequency on both the shock tube ground and the probe current perturbation.

Assuming this phenomena can be interpreted as an ion resonance, an estimate of the ion number density could be obtained. The predominant frequency observed on the ground is about 1.3 MHz (see figure 25). Solving the relation between frequency and number density (equation C3), the perturbation should occur at about

$$N_+ \sim 7 \times 10^9 \quad \{cm^{-3}\} \quad . \tag{C4}$$

Using the current collected, exclusive of the localized perturbations, as characteristic of the random thermal ionic current, (as given in equation C1), a value

$$N_+ \sim 2 \times 10^{11} \quad \{cm^{-3}\} \tag{C5}$$

is obtained at the perturbation.

It is amusing to use the ion-resonance effect as a calibration reference for the double probe. If the magnitude of the ion-saturated current is related to the ion density at the point corresponding to the density at ion resonance (C4), the probe current profile (dashed line) falls directly on the xenon ionic current profile of the mass spectrometer (using the spectrometer calibration constant discussed in Appendix B.3) as shown in figure 27. The location of the resonance-perturbation is indicated on the diagram.

APPENDIX D

TYPICAL EXPERIMENTAL PROCEDURE

Only one mass peak is observed during each run in the shock tube. A continuous time history of a particular ion abundance is obtained as the shock wave approaches the spectrometer sampling region. Sample oscillograms for two different mass peaks at the same initial conditions are shown in figure 22. The traces show the increase in a selected ionic current, the current reaching a maximum at shock reflection. Assuming the shock velocity U_s is constant in the time t represented by the oscillogram, the current at a particular distance x from the shock wave may be determined by the transformation $x = U_s t$. The scale between the traces shows the proper correspondence between the time coordinates in the oscillogram and the distance from the shock wave. The lower trace exemplifies the maximum sensitivity of the spectrometer.

To obtain a complete mass spectrum, several runs at the same initial conditions must be made. Use of a low resolution image slit permits large intervals of the spectrum (e.g., resolving power of 1 in 10) to be examined during a single run, defining areas of interest which should be studied with higher resolution.

The appropriate diaphragm and knife blades are installed, and the driver and test sections are mechanically pumped to a few microns. The driver is filled with the appropriate gas to over atmospheric pressure and the leak rate observed. The output from the spectrometer electron multiplier (using the movable electron-beam ion source) is displayed on an X-Y recorder, and the appropriate mass peak is resolved. The ion source is removed, exposing the sampling orifices to the shock tube, and the pressure in the shock tube is again measured. If naturally-occurring impurities are to be studied, the diffusion pump is closed off and the test section is allowed to leak and out-gas to the required level. If controlled amounts of known impurities are to be used, the impurity species are introduced simultaneously with the primary gas. If studies are to be made at the lowest possible impurity level, the test section is flushed with xenon and repumped with the diffusion pump. The primary gas (and impurities, if intended) is then introduced into the test section. To minimize the amount of impurities which leaks into the shock tube after introduction of the primary gas, the time elapsed between opening the control volume and bursting the shock tube diaphragm is kept as short as possible, usually less than one minute. The electronic instrumentation is rechecked (e.g., oscilloscopes, amplifiers,

noise levels, etc.) while the driver is being pressurized.

The precursor signal triggers one of the oscilloscopes which starts the remainder of the instrumentation sequence. The responses of the thin film gauges, the piezoelectric crystal, the double probe and the mass spectrometer are all displayed on oscilloscopes and recorded on Polaroid film.

A few microseconds after the shock wave reflects from sampling orifice diaphragm, a trigger signal from an oscilloscope pulses the draw-out electrode positively (to repel the large concentrations of ions generated by the reflected shock wave and thus protect the electron multiplier), turns off the accelerator and electron multiplier voltage, and initiates closure of the spectrometer valve.

APPENDIX E

THEORY OF PHOTOIONIZATION

A simplified version of the theoretical treatment of radiation-induced precursors in impure xenon will be presented. The analysis is similar to Dobbins' (Ref. 18) for pure argon and references to his work will be made freely. Radiative models will be developed along the lines of those of reference 44. The utilization of experimental data will be made whenever available, otherwise conservative estimates or assumptions will be used. The general problem of radiative energy transfer applicable to the present geometry will be presented, followed by a consideration of the various possible mechanisms for photoionization.

E.1 Ionization Ahead of a Strong Shock Wave

A strong shock wave propagates down a shock tube of circular cross section into an undisturbed gas. The frozen shock front (region of translational relaxation) is followed by a region of chemical non-equilibrium where ionization equilibrates with the translational degrees. This is followed by a highly ionized, strongly radiating zone in thermodynamic equilibrium, where the state of the shocked gas is given by equilibrium thermodynamics. The length of this equilibrium region is terminated by the cold driven gas (contact surface).

By neglecting the absorption and re-emission in the non-equilibrium region (the shock Mach numbers for the conditions to be considered insure that the relaxation time for ionization equilibrium will be brief, i.e., the non-equilibrium zone will be very short in length*) the radiation problem reduces to determining the ionization level in a cold gas flowing into a cylindrical volume of a radiating gas (in shock fixed coordinates) as shown in figure 16. The length d is the distance from the equilibrium ionization "front" to the contact surface in the shock tube, and U_s is the shock velocity. The symbols ① and ② refer to the region ahead of the shock and behind the shock (assuming immediate ionization relaxation), respectively.

As has been discussed, the presence of positive ions at large distances upstream of the shock wave can be attributed to photoionization caused by the intense radiation from the region downstream of the shock. The conservation equation for ions in the precursor region ahead of the shock is

$$-U_s \frac{dN_+}{dx} = R_{oi} N_A + R_{*i} N_* \qquad (E1)$$

where N_+, N_A, N_* are the ion, neutral atom, and excited atom number densities, respectively (the subscripts o, *,

*Typically, 3 cm in length; see L_R in Table 1.

and i symbolize the ground, excited, and ionized energy states of an atom). The R_{oi} source term is the photoionization rate (per ground state atom) from the ground state to the ionized state, and R_{*i} is the photoionization rate (per excited atom) from the excited state to the ionized state. For the flow velocities and densities under consideration, recombination in the precursor region may be ignored, so there is no sink term. On the left side of the equation, diffusion of ions from the shocked region and movement of the ions relative to the shock due to electric fields are neglected; the only term remaining is the expression for convection.

For the number of excited atoms ahead of a shock wave, another equation is needed; a similar conservation equation for excited state atoms is

$$-U_s \frac{dN_*}{dx} = R_{o*}\left(N_A\right) - R_{*o}\left(N_A\right)N_* \qquad \text{(E2)}$$

where R_{o*} is the photoexcitation rate (per unit volume) from the ground state (hence proportional to N_A). R_{*o} (de-excitation rate) is the Einstein coefficient for spontaneous emission multiplied by a suitable factor to include the effects of radiation trapping. In equation (E2) depletion by photoionization of excited state atoms has been neglected in comparison with the other terms.

Evaluation of the various rates requires a determination of the radiation intensity propagating ahead of the shocked gas. Using the configuration shown in figure 16 in the quasi-steady state, (i.e., the flow time scales are large compared with radiative time scales) radiation emanating from a small element in the shocked gas (equilibrium temperature and density are known) is considered. It can be shown (Ref. 44) that the average spectral intensity at a point on the axis and in front of the cylindrical slug of hot gas is given by

$$J(x) = \frac{1}{4\pi} \int_{\Omega} d\Omega \int_{0}^{d/\cos\theta} B_\nu \exp\left(\frac{-K_\nu'^{②} s}{\cos\theta}\right) \frac{K_\nu'^{②} ds}{\cos\theta} \exp\left(-K_\nu'^{①} x \sec\theta\right), \quad \text{(E3)}$$

which characterizes the complete radiation behavior for the given geometry (symbols are shown in figure 16). B_ν is the blackbody spectral intensity. $K_\nu'^{①, ②}$ are the effective absorption coefficients which include the absorption, and induced and spontaneous emission in the regions ① , ② (scattering is neglected). The last exponential term in the equation is due to the attenuation of radiation in the cold gas, (region ①). The remaining part of the integral gives the source of radiation in the hot gas.

The rates of photoionization and photoexcitation in equations (E1) and (E2) may now be found by using appropriate cross sections for the mechanisms involved and

the local radiation intensity from equation (E3). Consideration of solutions to the complete equations would give us an estimate of the ion number density as a function of distance from the shocked gas, for comparison with the experimental results. Such complete solutions are very lengthy and require strong assumptions especially because of the unavailability of experimental data, but considerations of portions of the complete equations yield interesting conclusions about the nature of precursors. In general, the equation may be divided into two main parts, one dealing with one-step photoionization of the primary gas and impurities, and the other considering photoexcitation and multi-step ionization of the primary gas.

E.2 One-Step Photoionization of Xenon and Impurities

Consideration of only the first term on the right hand side of equation (E1) allows the calculation of one-step photoionization, i.e., the rate of absorption of photons of sufficient energy to cause direct ionization of ground state atoms. Considering radiation with frequency higher than the frequency at the photoionizational edge (ν_{oi}) of a gas species, the rate of absorption per ground state atom of photons of frequency $\nu \geq \nu_{oi}$ is

$$R_{oi}(x) = 4\pi \int_{\nu_{oi}}^{\infty} \frac{J_\nu(x)}{h\nu} Q_{oi}(\nu) d\nu \quad , \qquad \text{(E4)}$$

where $J_\nu(x)$ is given by equation (E3), and $Q_{oi}(\nu)$ is the cross section for photoionization of the ground state atom. Substitution of equation (E4) into equation (E1) would yield the degree of ionization ahead of the shock wave; however, experimental data for K'_ν, the effective absorption coefficient, is virtually non-existant. It is at this point that assumptions must be made.

In the spectral region of interest, $\nu_{oi} \leq \nu \leq \infty$ (e.g., $\lambda_{oi} \sim 1000\text{Å}$), the product of absorption coefficient and depth of hot gas, d, will be large enough to permit the assumption that the shocked gas radiates as a black body, i.e., the region is optically thick. The integral over S will then yield only the blackbody spectral intensity. In the cold gas $K'^{①}_\nu \sim K^{①}_\nu$ (where $K^{①}_\nu$ is the absorption coefficient in the cold gas), i.e., self-emission can be neglected because the atomic excitation energies are much greater than the thermal energies of the gas ahead of the shock front so that $\frac{h\nu}{kT} \gg 1$ (discussion of the coefficients will be found in reference 44).

Certainly, at the high energies considered here, the blackbody photon distribution is dominated by the Boltzmann factor $\exp(-h\nu/kT)$, whatever the optical thickness. In the high energy limit (i.e., for $\nu \geq \nu_{oi} \gg \frac{kT}{h}$ ②) the Planck blackbody function may be written

$$B_\nu \sim \frac{2h\nu^3}{c^2} \exp(-h\nu/kT) \ .$$

Using the above assumptions and simplifications, equation (E3) may be written (expressing solid angles in terms of polar angles)

$$J_\nu(x) = \frac{B_\nu(T^{②})}{2} \int_0^{\theta_o} \sin\theta \, \exp\left(-K_\nu^{①} x \sec\theta\right) d\theta \qquad \text{(E5)}$$

where θ_o is the angle subtended from the axis to the edge of the shock (since only the shock front is now considered as the blackbody radiation source). Using equation (E5) in equation (E4) and considering only the first term in equation (E1) (i.e., one-step photoionization), and making suitable transformations, the ion number density may be written

$$N_+(\eta) = \frac{-4\pi R N_A}{U_s c^2} \int_\eta^{\eta_{max}} d\eta \int_{\nu_{oi}}^{\infty} \nu^2 \, Q_{oi}(\nu) e^{-h\nu/kT^{②}} d\nu \qquad \text{(E6)}$$

$$\cdot \left[\int_1^{\infty} \frac{e^{-\tau_\nu z}}{z^2} dz - \left(1 + \eta^{-2}\right)^{-\frac{1}{2}} \int_1^{\infty} \frac{e^{-\tau_\nu \left(1 + \eta^{-2}\right)^{\frac{1}{2}} \psi}}{\psi^2} d\psi \right]$$

where

$$\eta = \frac{x}{R}$$

$$z = \sec\theta = \left(1 + \eta^{-2}\right)^{\frac{1}{2}} \psi$$

$$\tau_\nu = K_\nu^{①} \eta R = Q_{oi}(\nu) \, N_A^{①} \eta R = \text{spectral optical depth.}$$

The integral over η arises from equation (E1) from which the ion distribution is found in the interval η (dimensionless number of radii upstream of the shocked gas) to η_{max} where η_{max} is the distance from the shocked gas at the time it is first formed to the location where the number density is observed (the boundary condition being $N_+(\eta_{max}) = 0$). Thus, η_{max} corresponds to a distance somewhat shorter than the shock tube length; however, calculations in which different values of the parameter are used, shows that the number density is fairly insensitive for values of $\eta_{max} > 100$.

Reflection and absorption of radiation from the walls of the shock tube would augment the radiation intensity in equation (E6). In general, the reflection coefficient will be a function of η , the radiation frequency, and the properties of the wall. Due to a lack of theoretical or experimental studies of this problem (especially in the ultraviolet spectral region considered here), this effect will necessarily be neglected. Certainly, the overall ionization level will be increased because of the additional photons available.

In considering the interaction between xenon and impurity gas, a "quenching" collision (between an excited xenon atom and a foreign gas molecule) in which some or all of the excitation energy is transferred to the impurity molecule is possible, resulting in a radiationless

de-excitation of the xenon atom. At the gas densities and velocities considered here, this effect will be neglected.

Several inferences may be made from equation (E6) about the general nature of the one-step photoionization mechanism. The exponential integral terms (in square parenthesis) in equation (E6) primarily represent attenuation in the cold gas due to absorption and $1/x^2$ decay due to shock tube geometry. The remaining portion represents the source of radiation at the shock front.

Thus far the formulation is general with regard to composition and may be used to calculate impurity as well as primary gas ionization levels. Substitution of the appropriate values (e.g., cross sections, temperature, etc.) give independent ion distributions, provided the cross section spectral intervals do not overlap. Experimental photoionization cross sections are available for xenon and several impurity gases, and the temperature in region ② can be determined from equilibrium thermodynamics. The initial number density is known and the shock velocity is found experimentally.

The most important parameter in the formulation is the optical depth τ_ν. The inverse of the optical thickness is a measure of the radiation mean free path, i.e., the average distance traversed by a photon of frequency ν before it is absorbed. If both the photoionization cross section and the neutral atom number density (initial

pressure) are large, the ion density falls off very rapidly from the shock front. If either the cross section or the number density is small, radiation will propagate further from the wave and the ion density profile will not be as steep. These features may be compared with the experimentally obtained profiles to determine the applicability of the one-step photoionization theory.

E.3 Photoexcitation and Multi-Step Photoionization of Xenon

Solution of the complete equation (E1) (including ionization from an excited state) requires knowledge of the distribution N_* of excited state atoms ahead of the shock wave, which, in turn, entails solving equation (E2). To evaluate the photoexcitation rate R_{o*}, the emission spectrum of xenon must be examined in more detail (see figure 15 for an energy-level diagram).

In the radiation model, xenon will be considered to exist either in the ground state $(5p^6\ {}^1S_0)$, in the first excited state $(5p^5\ 6s\ {}^3P_1)$, or in the ionic ground state $({}^2P^o_{3/2})$. Bremsstrahlung and continuum radiation from recombination (to the atomic ground state) of ions and electrons is strong ultraviolet radiation of sufficient energy (see figure 15) to photoionize ground state atoms which are considered in the section on one-step photoionization (Appendix E.2). In addition, the secondary continuum radiation due to recombination to an excited

state extends from the near ultraviolet (3357 Å) to higher frequencies.

The line radiation required for excitation of xenon atoms ahead of the shock comes from de-excitation of the first excited state in the shock-heated gas. This resonance radiation is readily absorbed in the equilibrium region of the shocked gas, and radiation originating at the rear of the volume of the hot gas will be absorbed before passing through the entire length of gas, i.e., the radiation propagating into the cold gas will emanate from a layer of gas close to the shock front. Therefore, in the frequency spectrum near the emission line the medium is optically thick, i.e., blackbody radiation may be assumed in the line emission region.

The cold gas will absorb the radiation in the core of the resonance line in a very short distance. Therefore radiation in the wings of the line (due to broadening effects in the hot gas) becomes of major importance, because it is this radiation that may propagate significant distances into the precursor region. Since high velocities exist behind the shock wave, the centers of the emission line (in the hot gas) and the absorption line (in the cold gas) may shift in frequency relative to each other due to Doppler effect. Dobbins finds this effect negligible for the velocities considered in argon. Since the velocities

in xenon are approximately the same (higher Mach number range in the present experiments is due to the lower sound speed in xenon), the Doppler shift will also be neglected here.

The rate of photoexcitation of ground state atoms is the photon flux multiplied by the absorption coefficient, integrated over the frequency interval of the emission line (ν_{*o}) ,

$$R_{o*} = 4\pi \int_{\nu_{*o}-\Delta}^{\nu_{*o}+\Delta} \frac{J_\nu(x)}{h_\nu} K_\nu^{①} \, d\nu \qquad \text{(E7)}$$

where $J_\nu(x)$ is the average spectral intensity at a point in the cold gas given by equation (E5) , which assumes blackbody radiation in the spectral region of interest. $K_\nu^{①}$ is the absorption coefficient (neglecting re-emission in the cold gas) and $\nu_{*o} \pm \Delta$ are the frequency limits of the broadened resonance line. $K_\nu^{①}$ will be controlled by the broadening mechanisms in the cold gas region. In the core of the absorption line, Doppler broadening (due to the thermal motion of the atoms) predominates, and the edges of the line are controlled by resonance broadening due to interactions of the radiating system with neutral xenon atoms. If the pressure of the absorbing gas is not too high, the form of the absorption line will be determined entirely by the wings (see, for example, reference 45).

The absorption coefficient for line radiation in the xenon gas ahead of the shock is

$$K_\nu^{①} = \left(\int_0^\infty K_\nu^{①} d\nu \right) \frac{\Delta\nu_R^{①}}{2\pi\left(\nu-\nu_{*o}\right)^2} \qquad \text{(E8)}$$

where $\Delta\nu_R^{①} = \frac{2}{3} \frac{e^2 f N_A^{①}}{m_e \nu_{*o}}$ (Ref. 46) is the resonance breadth (semi-half width) for low-pressure broadening including the effect of natural damping, and

$\left(\int_0^\infty K_\nu^{①} d\nu \right) = \frac{\pi e^2 f N_A^{①}}{2 m_e c}$ is the "integral absorption" relation (f is the oscillator strength, e the electronic charge, and m_e the electron mass).

Variation of impurity levels (for impurity levels less than 0.5%) produced no change in the xenon ion distribution determined from the mass spectrometric measurements. Thus, it is assumed that Van der Waals broadening and line shifting due to collisions with foreign gases may be neglected in the present calculations.

Substituting the appropriate expressions into equation (E7) for the photoexcitation rate,

$$R_{o*} = \frac{2\pi}{h\nu_{*o}} B_\nu\left(\nu_{*o}, T^{②}\right) \int_{\nu_{*o}-\Delta}^{\nu_{*o}+\Delta} \tau_\nu^{①} \cdot \left\{ E_2\left(\tau_\nu^{①}\right) - \left(1+\eta^{-2}\right)^{-\frac{1}{2}} E_2\left[\tau_\nu^{①}\left(1+\eta^{-2}\right)^{\frac{1}{2}}\right]\right\} d\nu \tag{E9}$$

where $\frac{B_\nu\left(\nu_{*o}, T^{②}\right)}{h\nu_{*o}}$ has been removed from under the integral due to its relatively slow variation with frequency over the limits of the integration. $\tau_\nu^{①} = K_\nu^{①} R\eta$ is again the spectral optical depth and

$$E_2(\tau_\nu) = \int_1^\infty \frac{\exp\left(-\tau_\nu z\right)}{z^2}\, dz$$

is the tabulated exponential integral. With an appropriate change of integration variable and by interchanging the order of integration, Dobbins was able to integrate the expression. Making use of his results, the rate may be expressed as

$$R_{o*} = \frac{4\pi}{3} \frac{B_\nu\left(\nu_{*o}, T^{②}\right)}{h\nu_{*o}} \left[\frac{\Delta\nu_R^{①}}{R}\left(\int_0^\infty K_\nu^{①} d\nu\right)\right]^{1/2} \cdot \left[\eta^{-1/2} - \eta^{-1/2}\left(1+\eta^{-2}\right)^{-3/4}\right] \tag{E10}$$

where the expression involving η gives the attenuation due to geometry and absorption in the cold gas.

The solution is of the form

$$N_*(x) \sim e^{kx} \int_x^\infty f(x') \, e^{-kx'} \, dx' \quad ,$$

however, using the condition that $\frac{dN_*}{dx} << 1$, an approximate solution valid except in close proximity to the shock is

$$N_*(x) \simeq \frac{R_{o*}(x)}{R_{*o}} \quad . \tag{E12}$$

Using appropriate values for xenon and experimental conditions in the shock tube (see Table 1), the excited state xenon number density (as a function of distance from the shock wave) may be determined.

The remaining rate in equation (E1) is R_{*i} , which involves the cross section for photoionization of an excited atom for photons of frequency $\nu \geq \nu_{i*}$,

$$R_{*i} = 4\pi \int_{\nu_{i*}}^\infty \frac{J_\nu(\nu, T^{(2)}) \, Q_*(\nu)}{h\nu} \, d\nu \quad . \tag{E13}$$

Although radiation of frequency $\nu \geq \nu_{i*}$ includes resonance line radiation at $\nu = \nu_{*o}$, the ratio of photoionization by resonance line radiation to photoionization by the secondary continuum will be small due to the magnitude of the cross section at that frequency and due to the small spectral interval at the resonance line.

The radiation propagating in the wings of the broadened emission line spectrum will be absorbed and re-emitted in the core of an emission line. This "thin" line secondary radiation will have a much higher probability of being absorbed in a shorter distance than the primary radiation. The effective loss of this radiation to the walls of the shock tube after repeated absorptions and re-emissions will be small provided the gas density is high enough or the radius of the shock tube is large enough. Holstein (Ref. 47) has considered this radiation "trapping." The trapping factor g_* gives the probability of escape of "imprisoned" photons in the gas for a cylindrical geometry. Multiplying by the Einstein spontaneous emission rate A_{*o} (inverse of life-time of excited state), the product is the effective de-excitation rate,

$$R_{*o} = g_* A_{*o} = \left[1.115\left(\frac{c}{3\pi^2 R\nu_{*o}}\right)^{\frac{1}{2}}\right]\left[\frac{8\pi^2 e^2}{m_e c^3}\frac{g_o}{g_*} f_{o*} \nu_{*o}^2\right] \quad \text{(E11)}$$

where R is the shock tube radius, f_{o*} is the oscillator strength, and g_* , g_o are the statistical weights of the excited and ground states, respectively.

Equation (E2) may now be solved for $N_*(x)$,

$$\frac{d\,N_*(x)}{dx} = \frac{R_{*o}}{U_s} N_*(x) - \frac{R_{o*}(x)}{U_s} \quad .$$

Therefore, this source of radiation will be neglected.

An evaluation must be made of the emission characteristics (in the appropriate frequency regime) of the shocked gas. Self-absorption in the hot gas will be almost negligible due to the transparency (small optical depth) at frequencies $\nu \sim \nu_{i*}$ ($\lambda_{i*} = 3357$ Å), and absorption in the cold gas will be almost totally absent. Thus, for the secondary continuum, $K_\nu'^{②}S = K_\nu^{②}S \ll 1$ and $K_\nu'^{①}x = K_\nu^{①}x \ll 1$ and equation (E3) may be written

$$J_\nu(x) = \frac{1}{4\pi}\int_\Omega d\Omega\ B_\nu\ K_\nu^{②}\frac{d}{\cos\theta} \quad .$$

Since absorption is very small in the cold gas, it will be assumed that the precise shock tube radiation model is dominated by the inverse square law attenuation characteristic of radiating sources. This assumption is supported by Dobbins' more rigorous treatment with argon. The average intensity at a point ahead of the radiation region with length, d, is then

$$J_\nu(\eta) = \frac{B_\nu\left(\nu,\ T^{②}\right)}{2}\ K_\nu^{②}\ d\ \frac{1}{\eta^2} \quad . \qquad \text{(E14)}$$

As the temperature in the shocked gas is very high, the population of the upper bound states is large and the overlapping of absorption continua is excessive. In this region the total absorption coefficient, $K_\nu^{②}$, is given

by a Kramers-Unsöld type equation (Ref. 44)

$$K_\nu^{②} = \frac{32\pi^2 e^6 kT^{②} N_A^{②}}{3\sqrt{3}\, h^4 c} \frac{1}{\nu^3} \exp\left(\frac{-h\nu_{io}}{kT^{②}}\right) \left[\exp\left(\frac{h\nu}{kT}\right)-1\right] \xi\left(\nu, T^{②}\right) \qquad \text{(E15)}$$

where e , k , h , c are physical constants and $\xi(\nu, T)$ is a quantum-mechanical correction factor.

The absorption cross section for xenon excited to the $n^{\underline{th}}$ level, according to a Kramers' law formulation (see for example, reference 31) is given by

$$Q_*\left(\nu_{i*}\right) = \frac{64\pi^4 m_e e^{10}}{3\sqrt{3}\, h^6 c n^5} \frac{1}{\nu_{i*}^3} g_f \qquad \text{(E16)}$$

where g_f is the Gaunt factor, which gives the quantum mechanical departure from the hydrogenic approximation, and n is the effective principal quantum number for the excited state. Very recently Schlüter (Ref. 27) has studied the values of g_f and $\xi(\nu, T)$ for xenon using the quantum defect method. The temperatures and frequencies he considers are applicable to the present experimental conditions. Extrapolating his curves for $\xi(\nu,T)$ a value of g_f may be found such that when substituted into equation (E16) the absorption cross section for xenon excited to the first state is

$$Q_*\left(\nu_{i*}\right) = 4.81 \times 10^{-19} \left\{cm^2\right\} \quad .$$

For higher frequencies, the cross section is expressed (Ref. 44)

$$Q_* \left(\nu > \nu_{i*}\right) = Q_* \left(\nu_{i*}\right)\left(\frac{\nu_{i*}}{\nu}\right)^3 \quad .$$

The absorption coefficient may be combined with the Planck function in equation (E14) so that the photo-ionization rate expressed in equation (E13) becomes

$$R_{*i} = \frac{128\pi^3 e^6 kT^{②}}{3\sqrt{3}\, h^4 c^3} \exp\left(\frac{-h\nu_{io}}{kT}\right) \frac{N_A^{②} d}{\eta^2} \cdot Q_*\left(\nu_{i*}\right) \int_1^\infty \left(\frac{\nu_{i*}}{\nu}\right)^4 \xi\left(\nu, T^{②}\right) d\left(\frac{\nu}{\nu_{i*}}\right) \tag{E17}$$

Substituting the appropriate values, equation (E1) may now be integrated to give the total ion density as a function of distance ahead of a strong shock wave (see Part IV).

REFERENCES

1. Lasher, L. E. and Wilson, K. H., AIAA J. 6, 2419 (December, 1968).

2. Lin, S. C., Goldberg, W. P., and Janney, R. B., Avco-Everett Research Laboratory, Research Rpt. 127 (1962).

3. Hollyer, R. N., Jr., Preliminary Studies in the APL High Temperature Shock Tube, Johns Hopkins University Appl. Physics Lab., Rpt. No. CM-903 (1957).

4. Groenig, H., Phys. Fluids 6, 142 (1963).

5. Weymann, H. D., Phys. Fluids 4, 545 (1960).

6. Weymann, H. D. and Troy, B., Bull. Am. Phys. Soc. 6, 212 (1961).

7. Gloersen, P., Phys. Fluids 3, 857 (1960).

8. Holmes, L. B., Plasma Density Ahead of Pressure Driven Shock Waves, University of Rochester, TN 1 (May 1966).

9. Lederman, S. and Wilson, D.S., AIAA J. 5, 70 (1967).

10. Wilson, D. S. and Lederman, S., Precursor Ionization Due to Photoionization of H_2 Impurities in Argon Shocks, Polytechnic Institute of Brooklyn, PIBAL Rpt. No. 1033 (November 1967).

11. Mulac, A. J., "Experimental and Theoretical Investigation of Shock Tube Precursors," NASA-CR-97190 (September 1968).

12. Pipkin, A. C., Phys. Fluids 4, 1298 (October 1961).

13. Wetzel, L., AIAA J. 2, 1208 (July 1964).

14. Appleton, J. P., Phys. Fluids 9, 336 (February 1966).

15. Ferrari, C. and Clarke, J. H., "On photoionization ahead of a strong shock wave," in Supersonic Flow, Chemical Processes, and Radiative Transfer, edited by D. B. Olfe and V. Zakkay, Pergamon Press, New York (1964).

16. Murty, S. S. R., J. Quant. Spectrosc. Radiat. Transfer 8, 531 (1968).

REFERENCES (cont.)

17. Biberman, L. M. and Veklenko, B. A., JETP 37, 117 (1960).

18. Dobbins, R. A., Photoexcitation and Photoionization of Argon Ahead of a Strong Shock Wave, AIAA Paper No. 68-666 (1968).

19. Wilson, D. S. and Lin, T. C., Impurity Ionization Theory of Precursors, Polytechnic Institute of Brooklyn, PIBAL Rpt. No. 1006 (October, 1966).

20. Sturtevant, B., J. Fluid Mech, 25, 641 (1966).

21. Petschek, H. and Byron, S., Annals of Phys. 1, 270 (1957).

22. Smith, J. A., Coles, D., Roshko, A., and Prasad, A. J., Graduate Aeronautical Laboratories, California Institute of Technology Report FM-67-1 (1967).

23. Smith, J.A., Phys. Fluids 11, 2150 (October, 1968).

24. Handbook of Chemistry and Physics, Forty-third Edition, The Chemical Rubber Publishing Co., Cleveland, Ohio, 1962.

25. Moore, C. E., "Atomic Energy Levels," N. B. S. Circular 367 1, 211 (June 15, 1949).

26. Wilkinson, P. G., J. Quant. Spectrosc. Radiat. Transfer 6, 823 (1966).

27. Schlüter, D., Zeitschrift für Physik 210, 80 (1968).

28. Sampson, J. A. R. and Kelley, F. L., "III: Photoionization Cross Sections of the Rare Gas,"

29. Cook, G. R. and Metzger, P. H., J. Chem. Phys. 41, 321 (1964).

30. Arave, R. J., "Thermodynamic and Normal Shock Properties of the Inert Gases in Ionization Equilibrium," Boeing Report D 2-22291 (October, 1963).

31. Marr, G. M., Photoionization Processes in Gases, Academic Press, New York (1967).

32. Biberman, L. M. and Yakubov, I. T., Soviet Physics-Technical Physics 8, 1001 (May 1964).

REFERENCES (cont.)

33. Nelson, H. F., "Structure of Shock Waves with Nonequilibrium Radiation and Ionization," Purdue University, AA&ES 68-5 (June 1968).

34. Clarke, J. H., and Onorato, M., "Asymptotic Solutions of Normal Shock Waves Structured by Nonequilibrium Radiative and Collisional Ionization," Brown University Rpt. No. Nonr-562(35)/22 (March 1969).

35. Roshko, A. and Baganoff, D., Phys. Fluids 4, 1445 (1961).

36. Jahn, R. G. and Weimer, D., J. Appl. Phys. 29, 741 (1958).

37. Hayes, W. D. and Probstein, R. F., Hypersonic Flow Theory, Academic Press, New York (1959).

38. Wang, C. C. P., Ph.D. Thesis, California Institute of Technology (1967).

39. Johnson, E. O. and Malter, J., Phys. Rev. 80, 58 (1950).

40. Radcliffe, S. W., McLaren, T. I., and Hobson, R. M., "Probe Measurements of Charged Particle Concentrations and Ionization Relaxation Phenomena in Low Density Supersonic Gas Flows," 30th Propulsion and Energetics Panel Meeting, Munich (September, 1967).

41. Harp, R. S. and Crawford, F. W., J. Appl. Phys. 35, 3436 (1964).

42. Kato, K., Ogawa, K., Yoseli, M., and Shimahara, H., J. Phys. Soc. Japan 18, 1849 (1963).

43. Toepfer, A. J. and Comisar, G. G., "Observations of a Resonance Probe Effect Near the Ion Plasma Frequency," Aerospace Report TR-1001 (9220-04)-1 (October, 1966).

44. Zel'dovich, Ya. B. and Raizer, Yu. P., Physics of Shock Waves and High-Temperature Hydrodynamic Phenomena, Vol I, English translation edited by W. D. Hayes and R. F. Probstein, Academic Press, New York 135 (1966).

45. Mitchell, A. C. G. and Zemansky, M. W., Resonance Radiation and Excited Atoms, Cambridge Press, London (1934).

REFERENCES (cont.)

46. Breene, R. G., Jr., "Line Width," in Hand-buch der Physik, Band XXVII, Spectroskopie I, Springer Verlag, Berlin (1946).

47. Holstein, T., Phys. Rev. 72, 1212 (1947).

TABLE 1

TEST CONDITIONS AND PARAMETERS
FOR TYPICAL EXPERIMENTS IN XENON
(Refs. 23, 25, 26, 28, 29, 30)

	XENON		Oxygen
	Low Pressure	High Pressure	Impurity
P_1 (torr)	0.120	0.500	0.0005
T_1 (^oK)	300	300	300
N_{A1} (cm^{-3})	3.9×10^{15}	1.6×10^{16}	1.6×10^{13}
λ_1 (cm)	4.4×10^{-2}	1.1×10^{-2}	
M_s	18.5	15.2	18.5
T_{2e} (^oK)	9800	9500	9800
α_{2e}	0.36	0.20	
U_s (cm/sec)	3.3×10^5	2.7×10^5	3.3×10^5
ionization relaxation length L_R(cm)	3	3	
photon mean free path $l_{oi}(\nu_{oi})$(cm)	4.3	1.0	1.3×10^4
$Q_{oi}(\nu_{oi})(cm^2)$	60×10^{-18}	60×10^{-18}	5×10^{-18}

---

m/e = 131 Spectrometer Settings

Spectrometer Draw-Out Voltage = 44 volts

Magnetic Field = 4000 gauss

Acceleration Potential = 1900 volts

Number of Orifices = 12

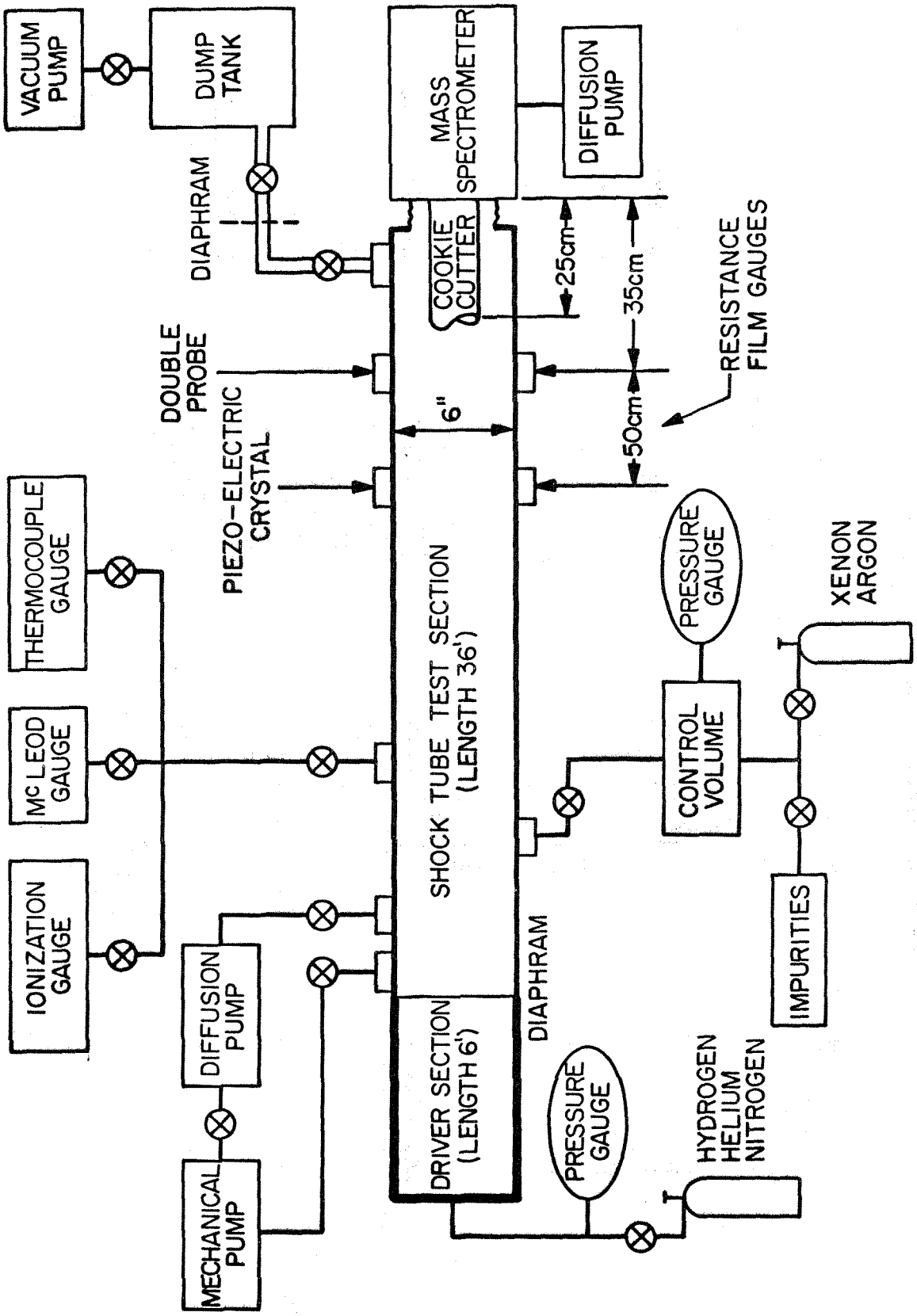

Figure 1. Schematic Diagram of the Apparatus

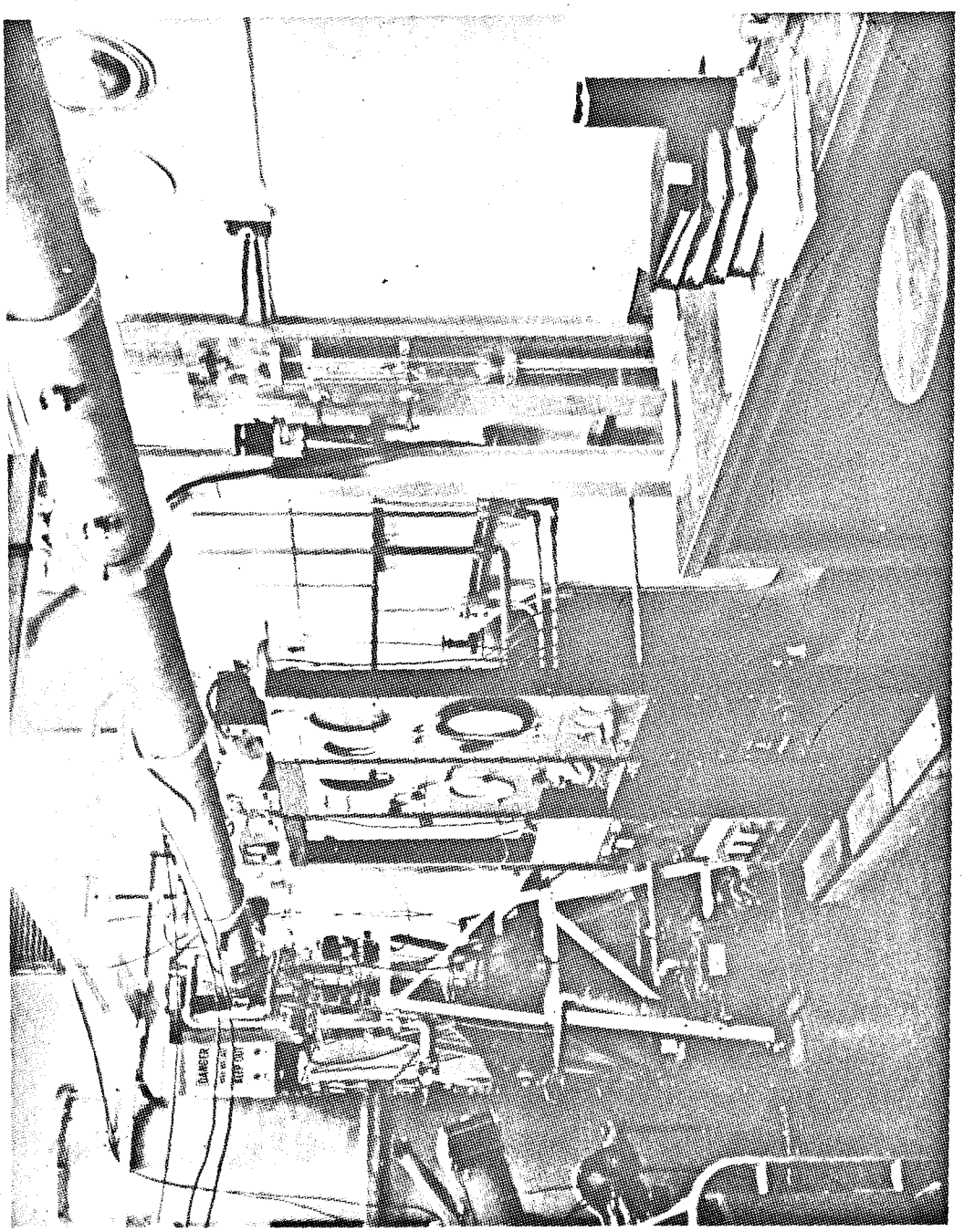

Figure 2. GALCIT 6" Shock Tube Test Section

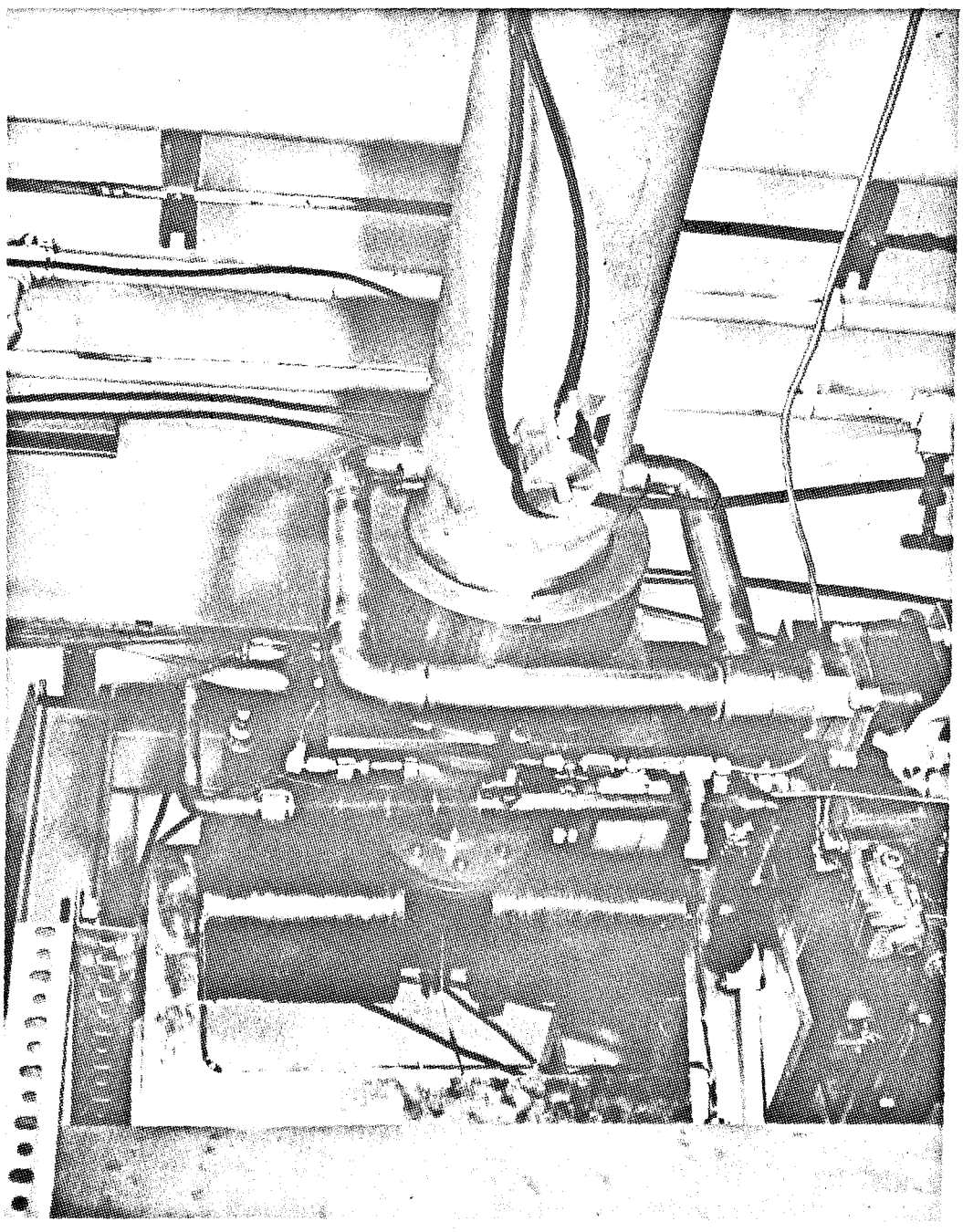

Figure 3. Mass Spectrometer Installation at the End of the Shock Tube

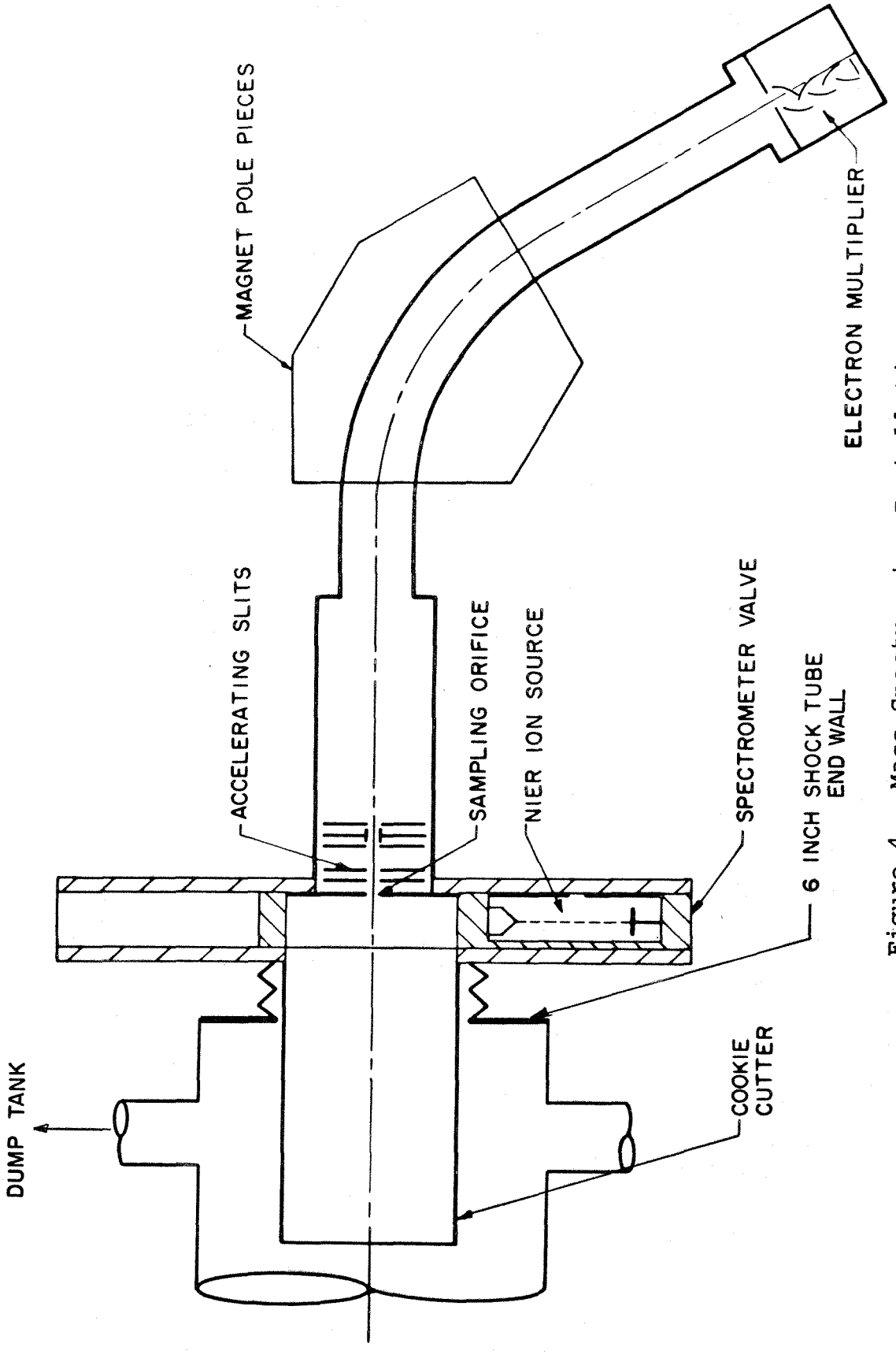

Figure 4. Mass Spectrometer Installation

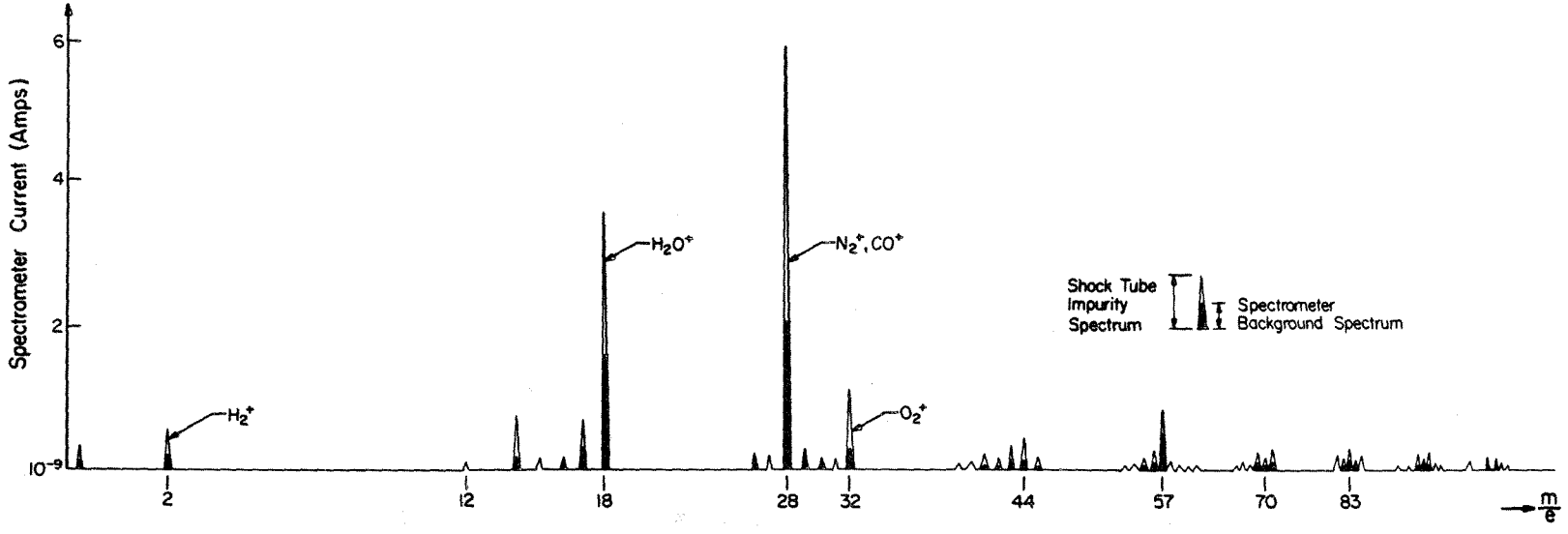

Figure 5. Schematic Representation of a Mass Spectrum of Impurities in the 6" Shock Tube

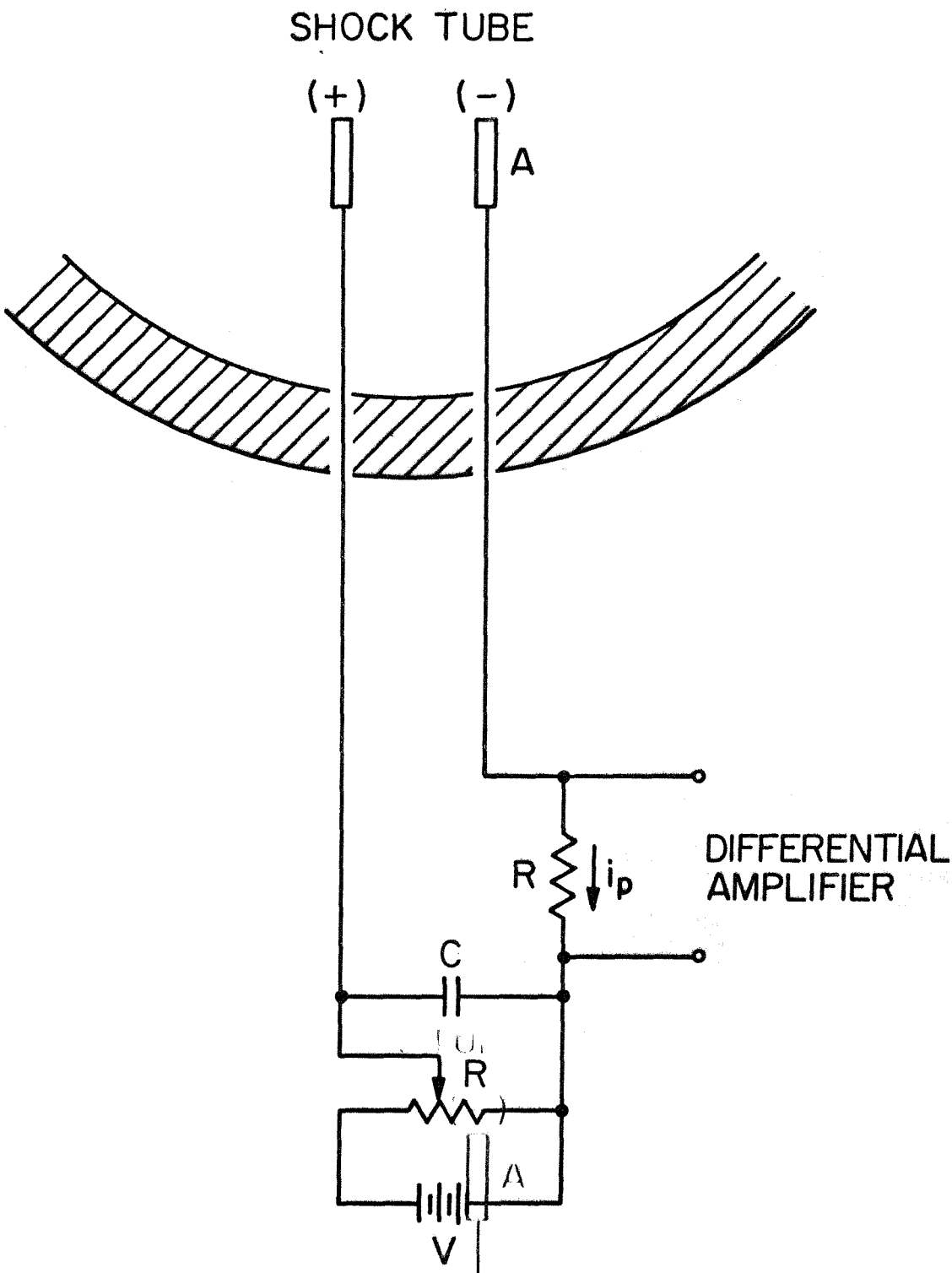

Figure 6. Langmuir Double Probe Schematic

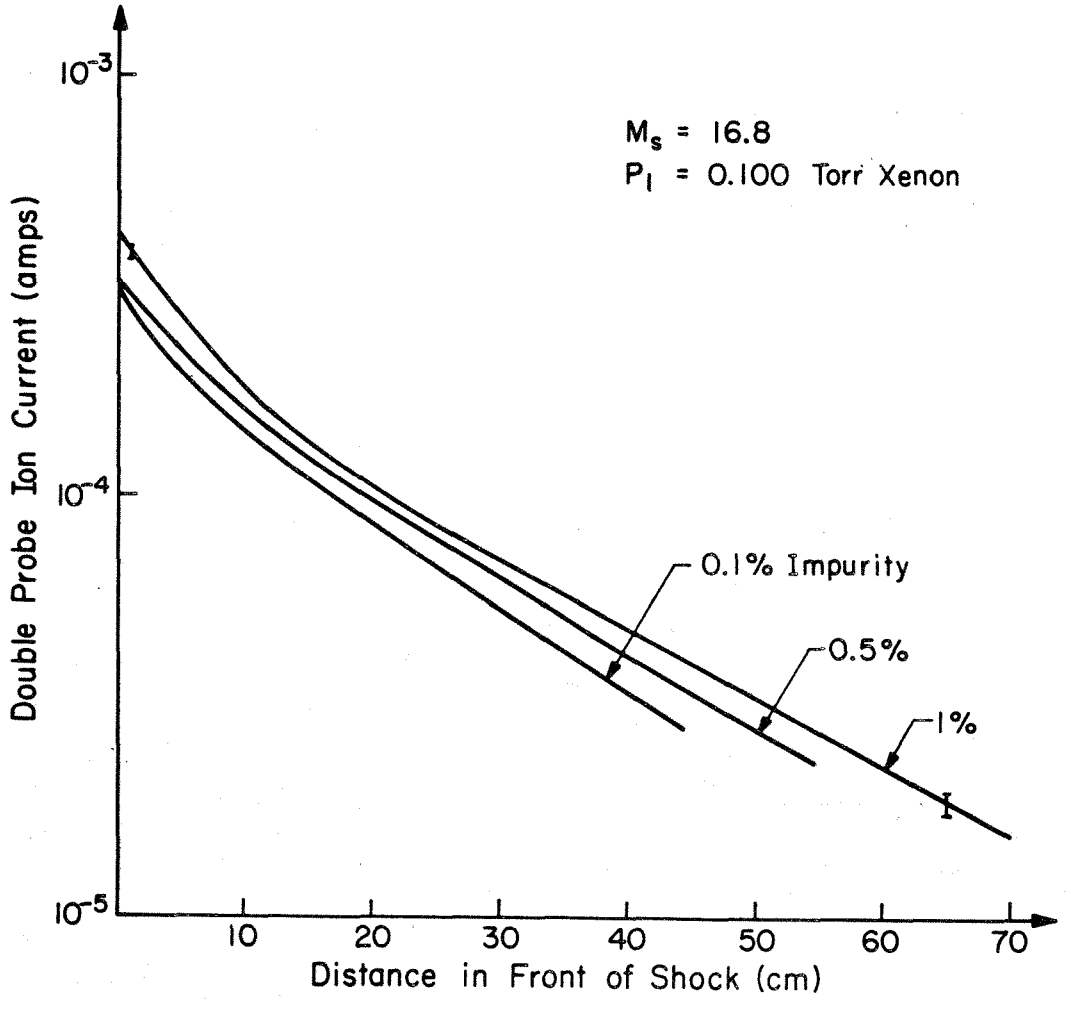

Figure 7. Probe Ion Current Profiles Showing the Effect of Variation of Impurity Levels

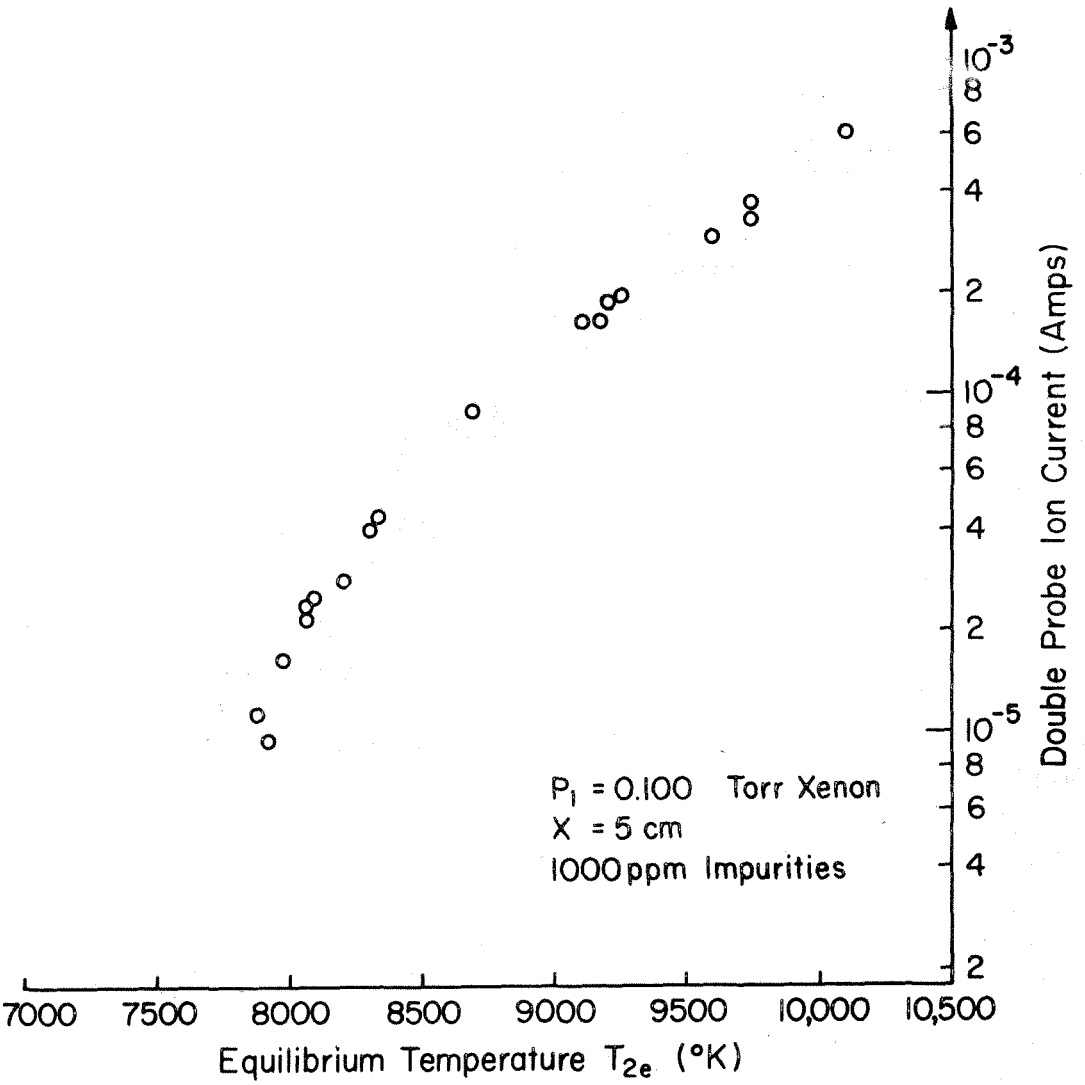

Figure 8. Probe Ion Current at a Distance of 5 cm as a Function of Equilibrium Temperature behind the Shock

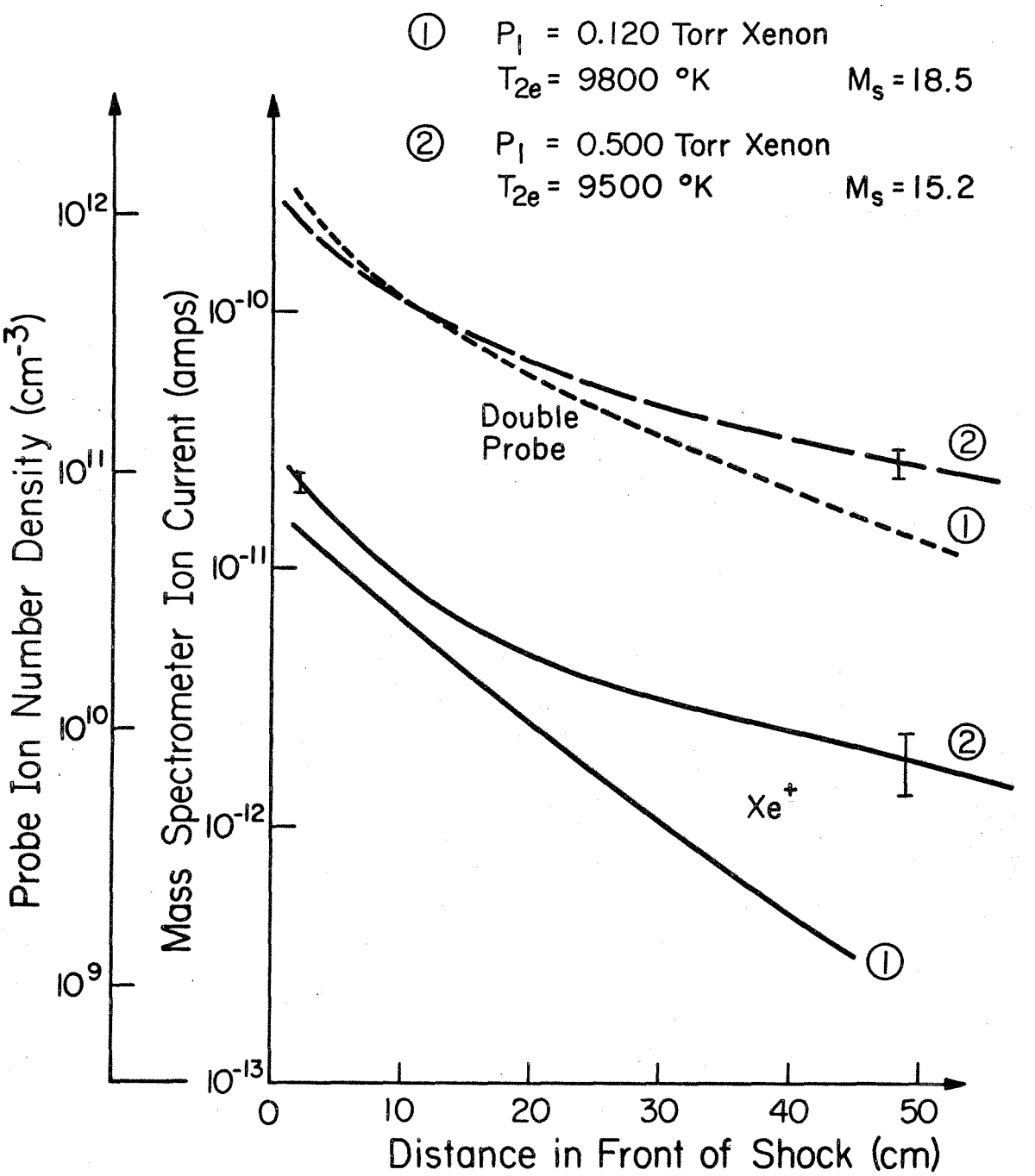

Figure 9. Comparison of Ion Number Density Determined from Double Probe Currents and Xenon Ionic Currents Obtained from Mass Spectrometric Data for Two Different Initial Pressures

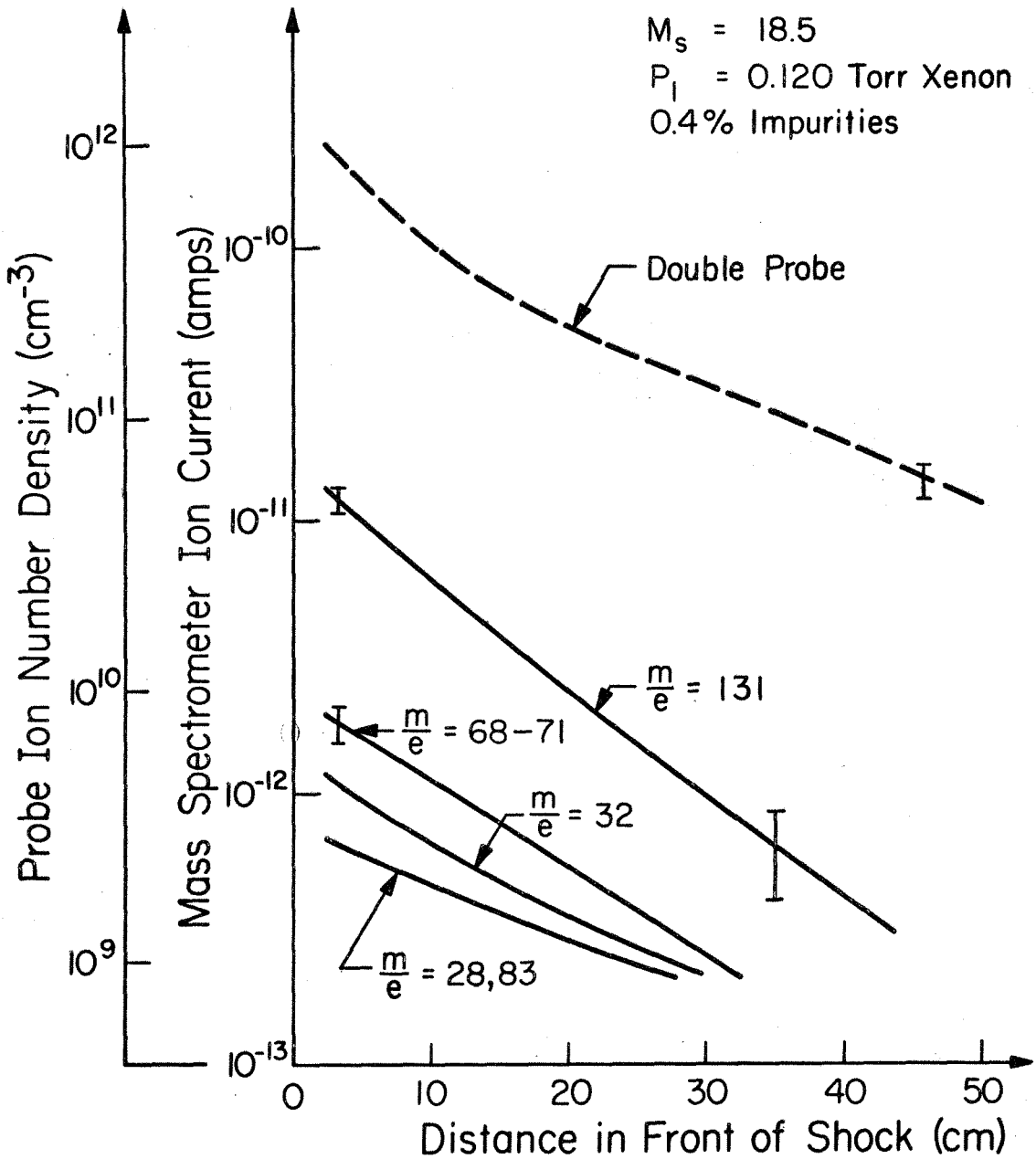

Figure 10. Schematic of Probe-Measured Ion Density and Spectrometer-collected Ion Currents as a Function of Distance from the Shock Wave (Low Pressure)

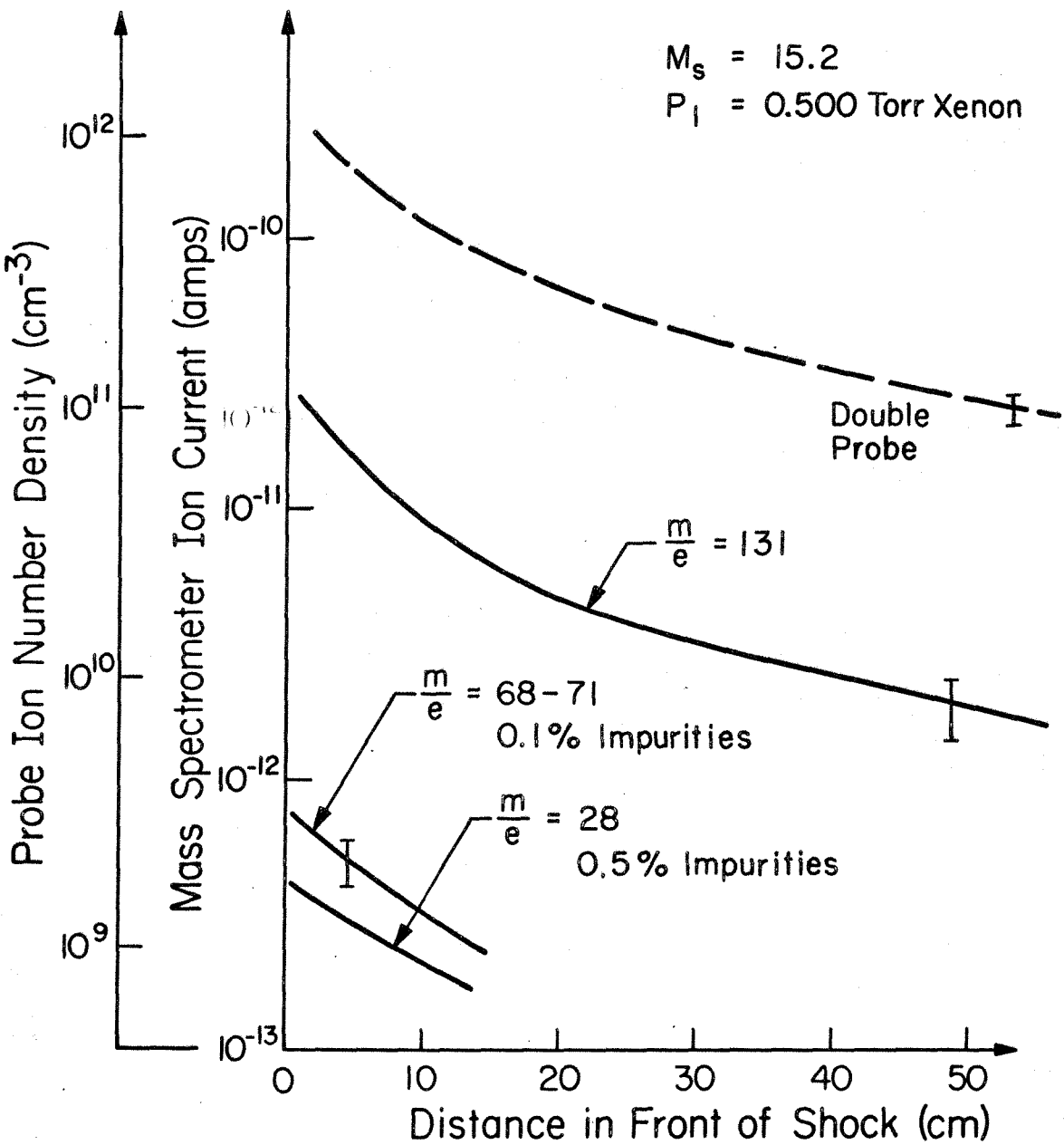

Figure 11. Schematic of Probe Measured Ion Density and Spectrometer-Collected Ion Currents as a Function of Distance from the Shock Wave (High Pressure)

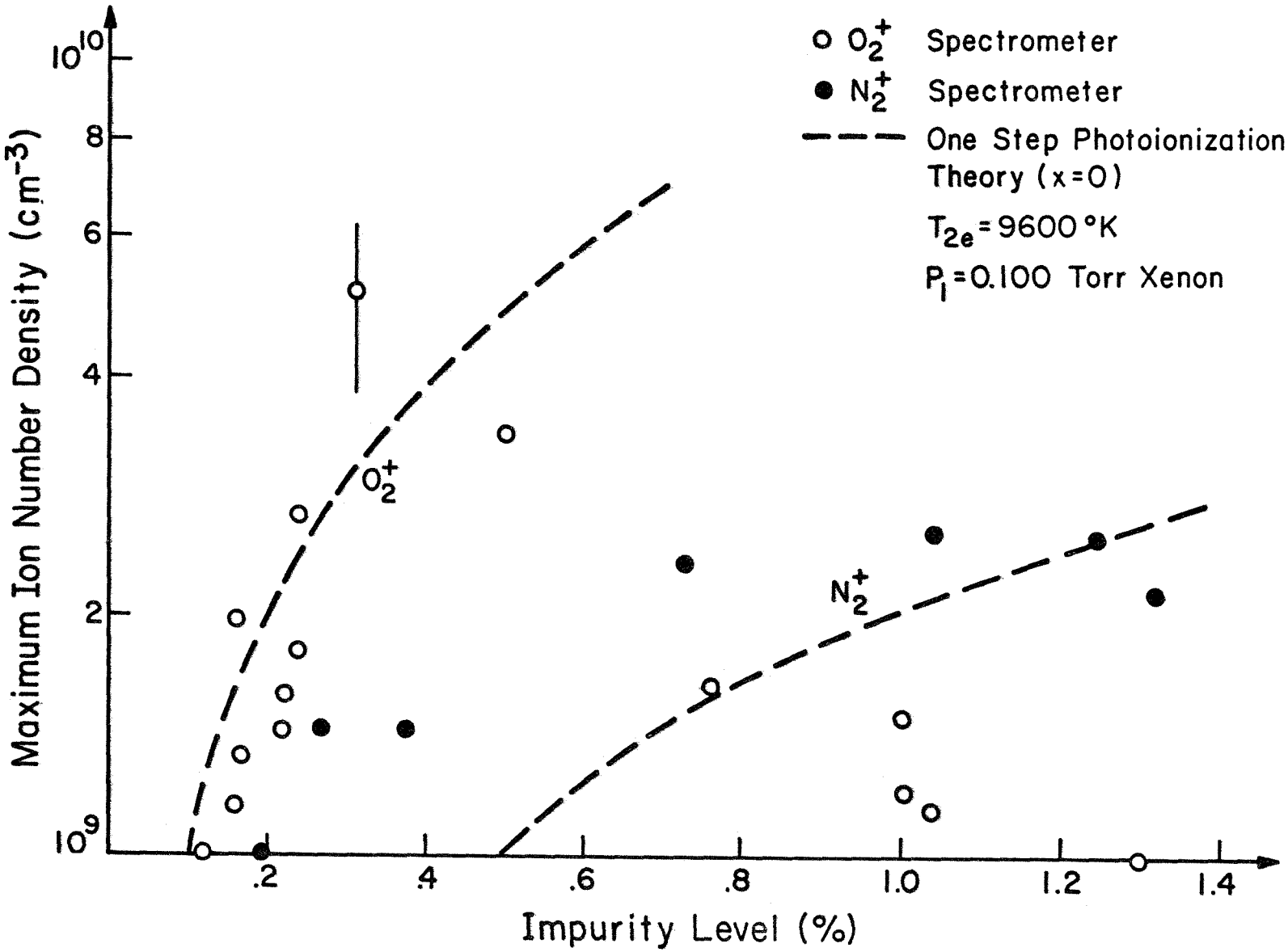

Figure 12. Comparison of One-Step Photoionization Theory with Maximum Spectrometer Currents for Injection of Molecular Oxygen and Nitrogen in Pure Xenon

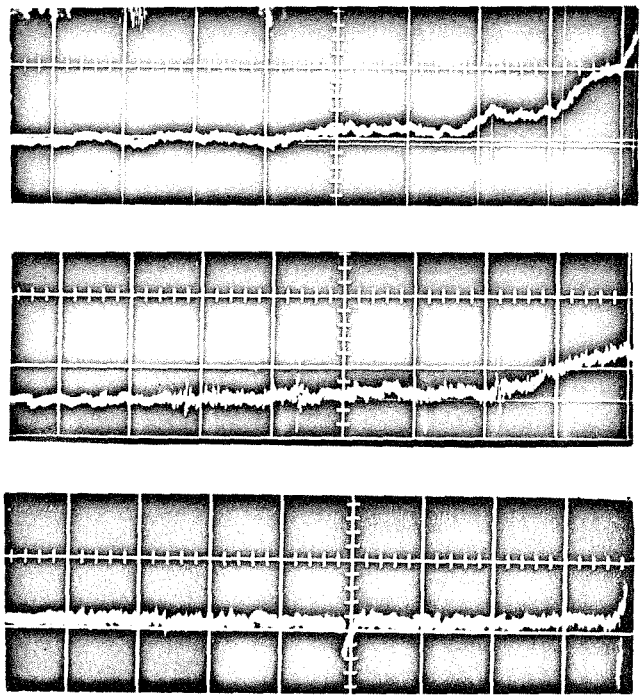

Figure 13. Spectrometer Oscillograms Showing Decrease in Xenon Current Due to Addition of Large Amounts of Impurities

Sensitivity: 5×10^{-12} amp/div
Sweep Rate: 20 μsec/div

$M_s = 17$

$P_1 = 0.100$ torr xenon

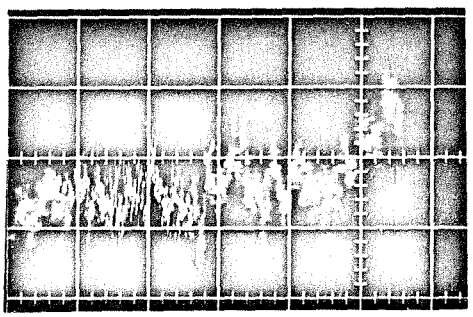

$M_s = 12.2$

$P_1 = 0.100$ torr argon

Figure 14. Argon Ionic Current Collected by the Spectrometer

Sensitivity: 1×10^{-12} amp/div
Sweep Rate: 20 μsec/div

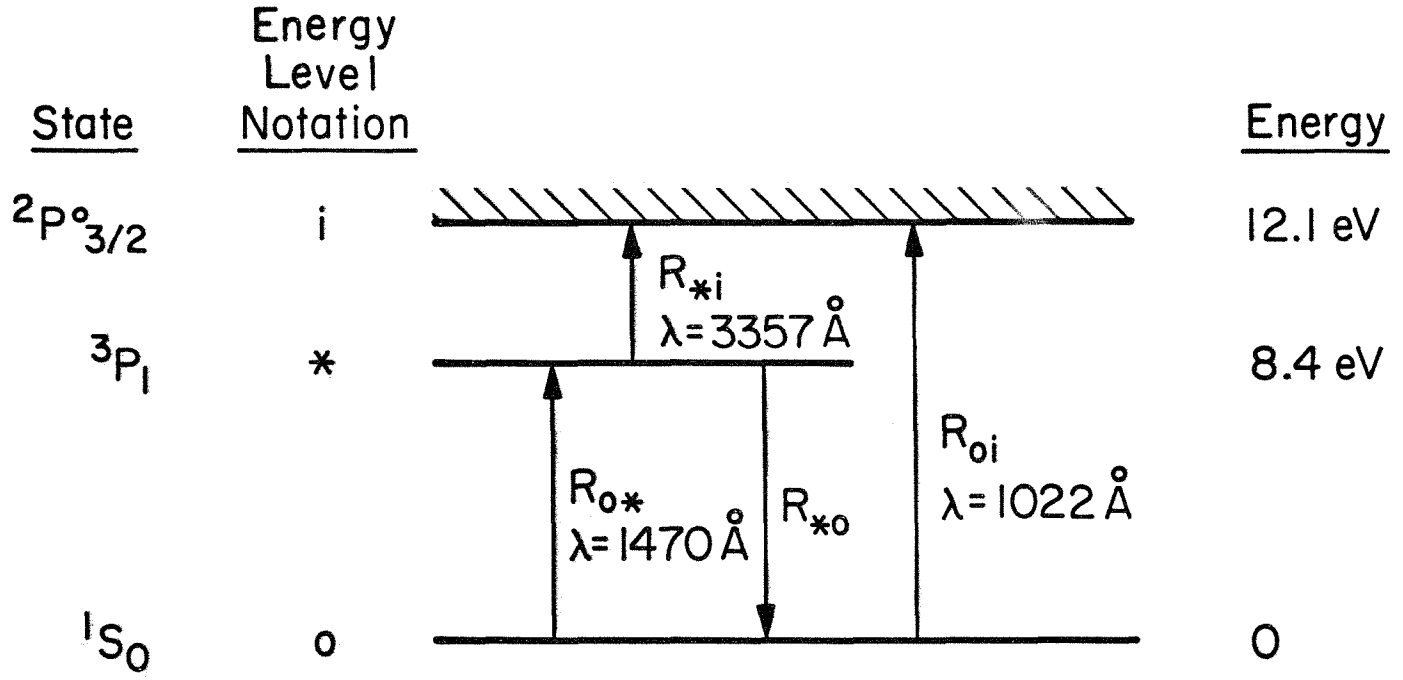

Figure 15. Simplified Schematic of Xenon Energy Levels and Rates

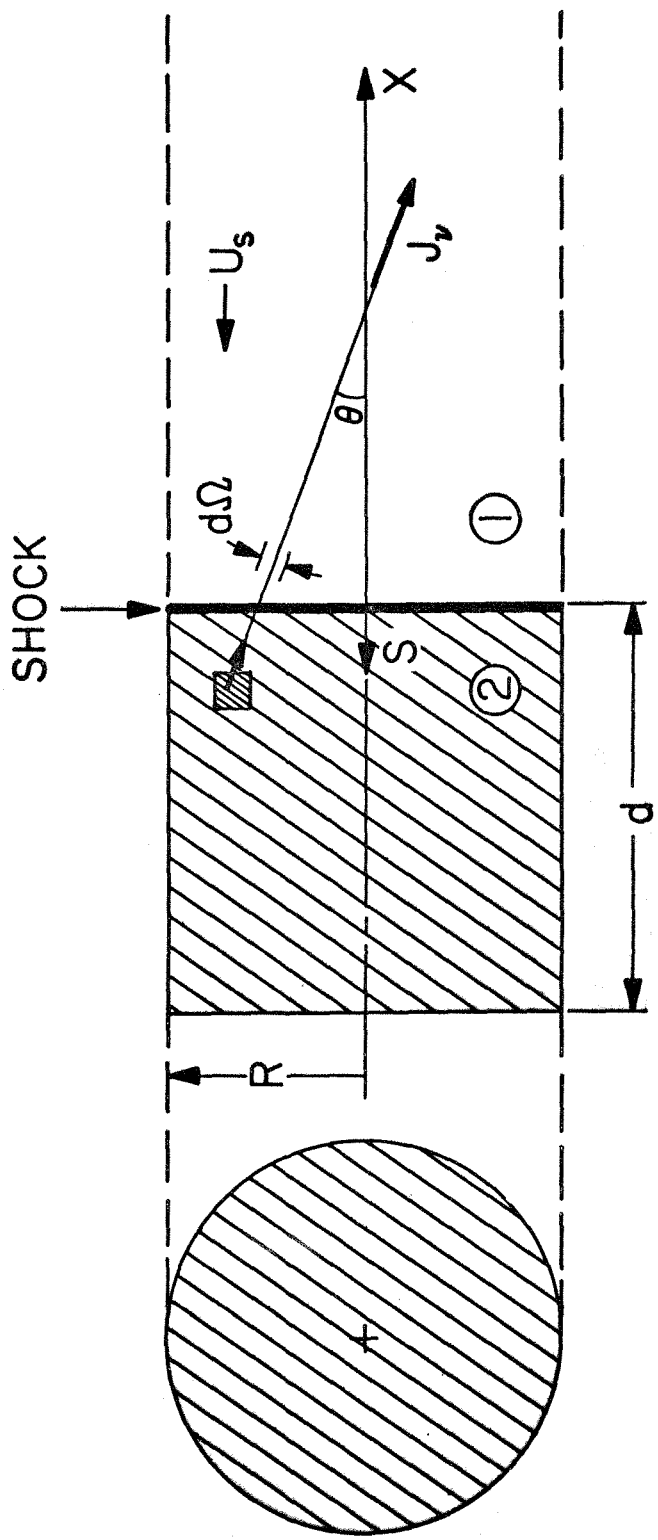

Figure 16. Shock Tube Radiation Model in Shock-Fixed Coordinates

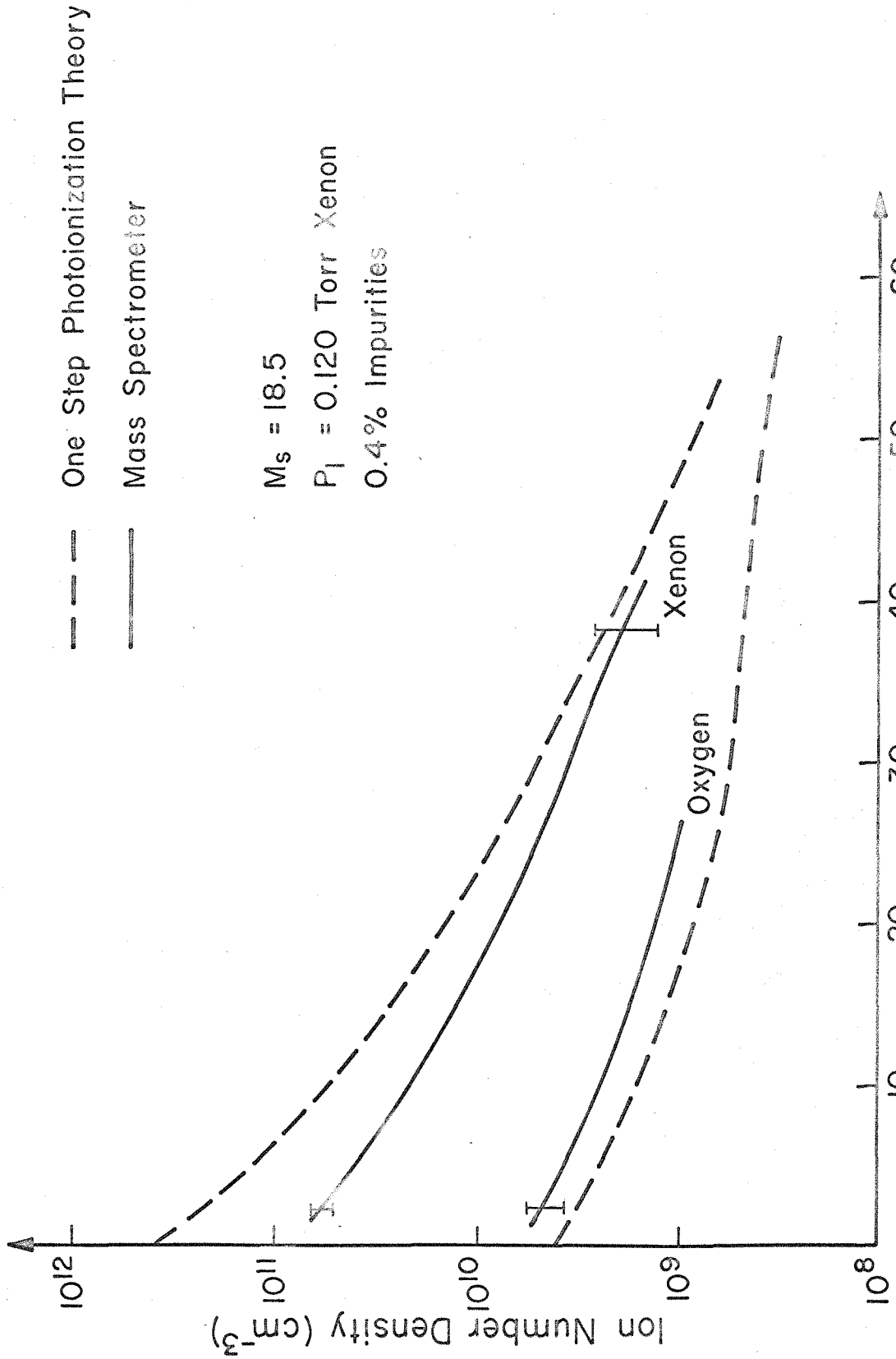

Figure 17. Comparison between Experimental Spectrometer Measurements and One-Step Photoionization Theory for Low Initial Pressure

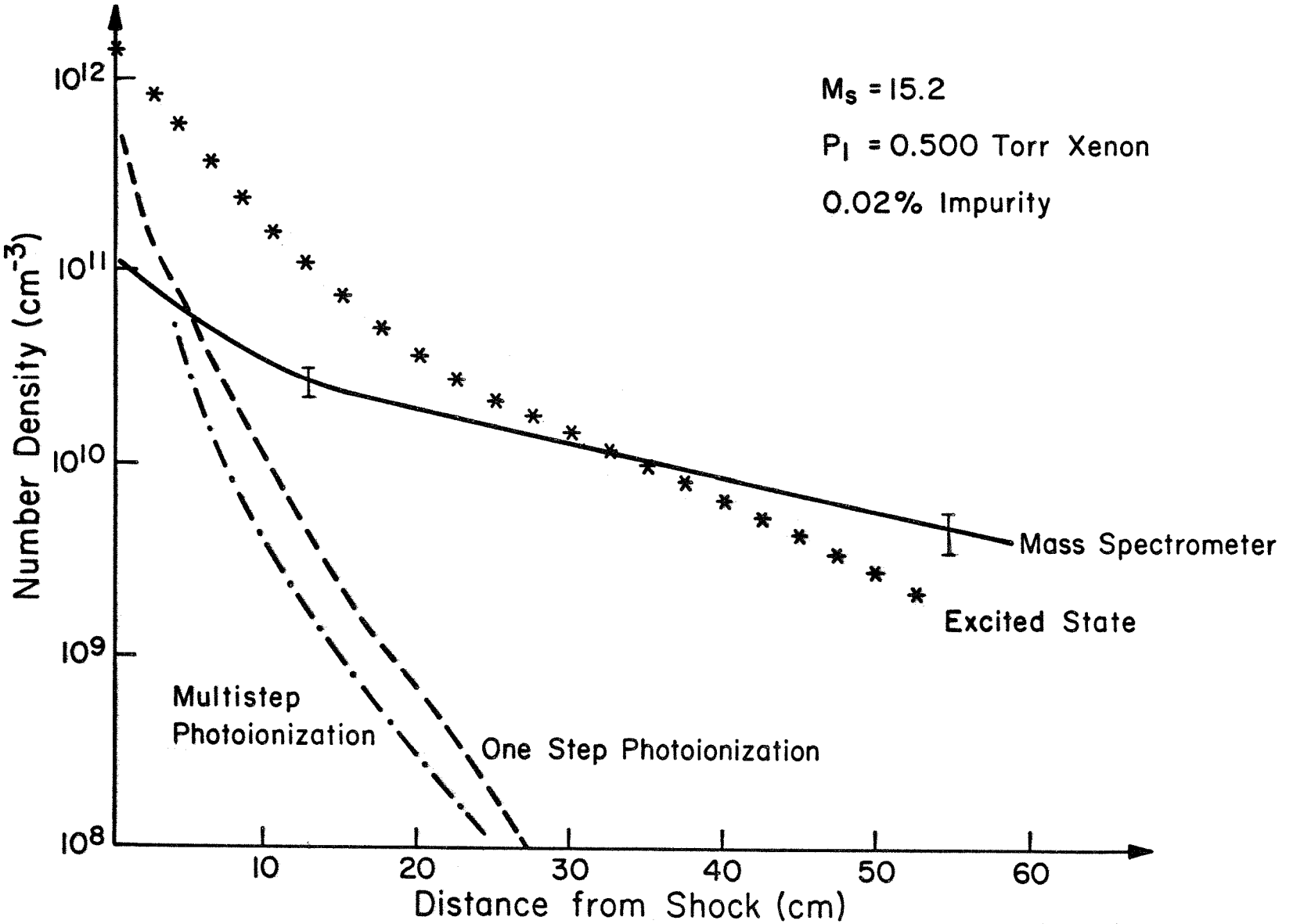

Figure 18. Comparison between Experimental Spectrometer Measurements and Theory for High Initial Pressure

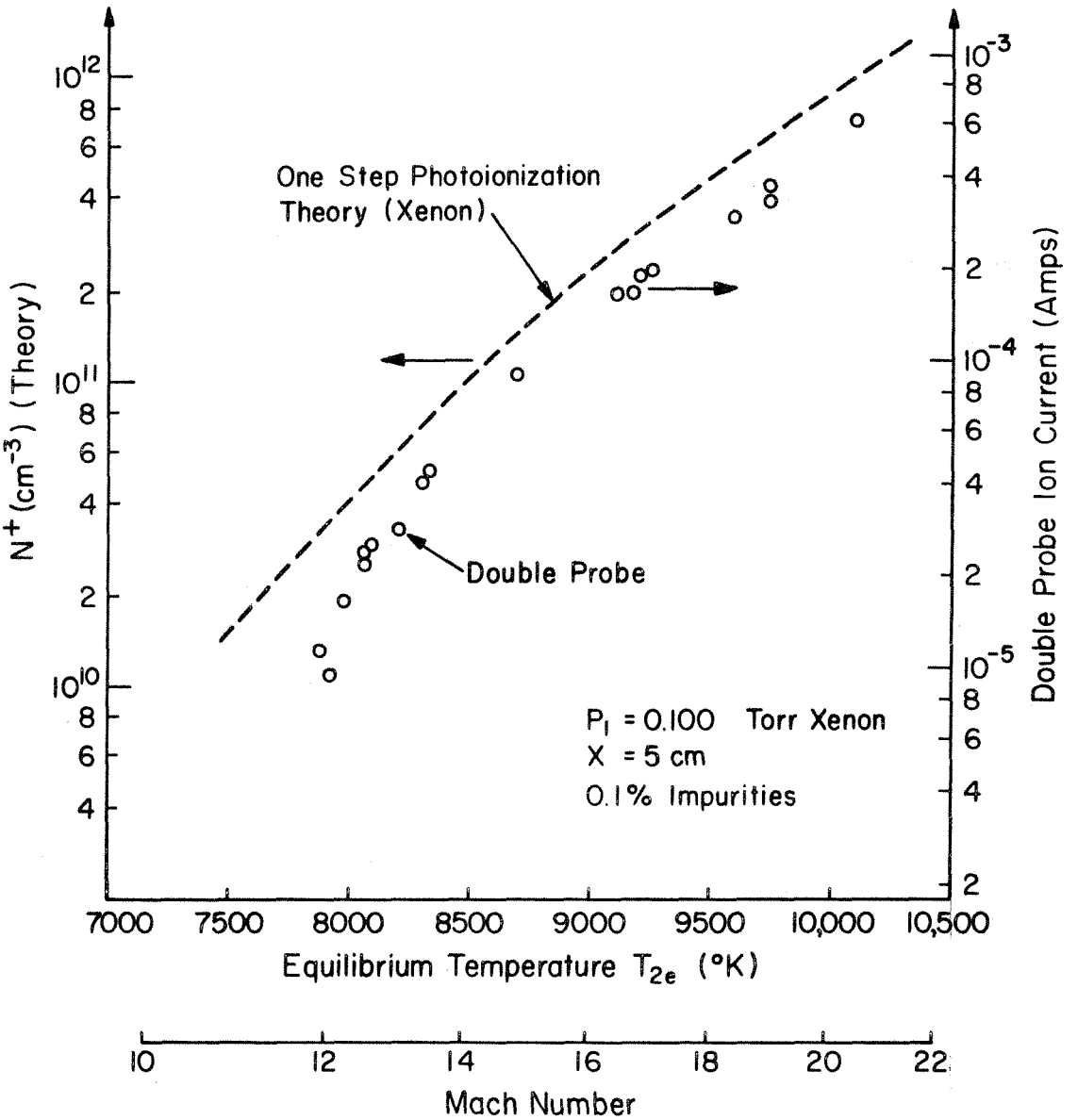

Figure 19. Profile Comparison between One-Step Photoionization Theory and Double Probe Data as a Function of Temperature behind the Shock and Mach Number

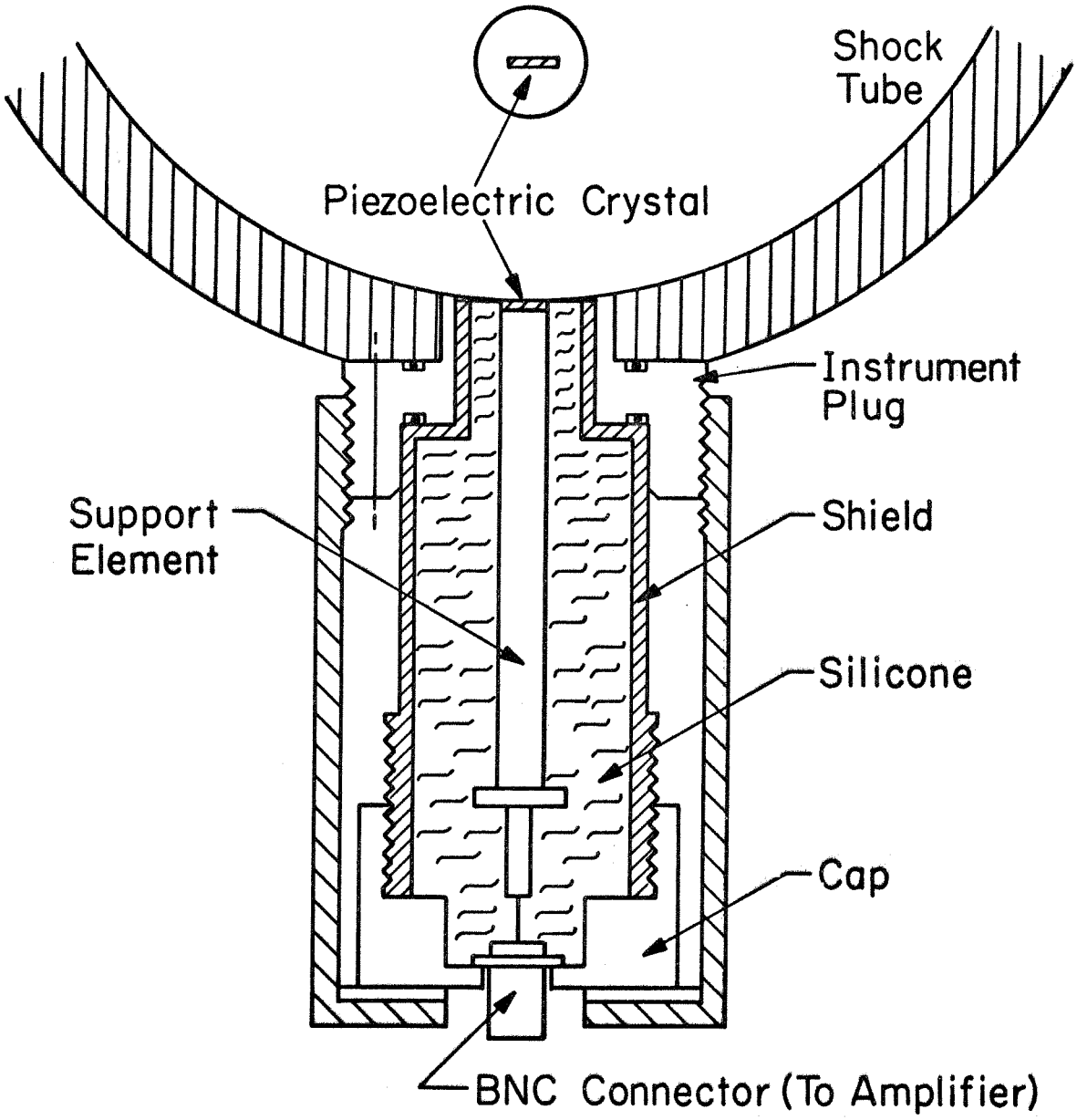

Figure 20. Schematic of Piezoelectric Detector

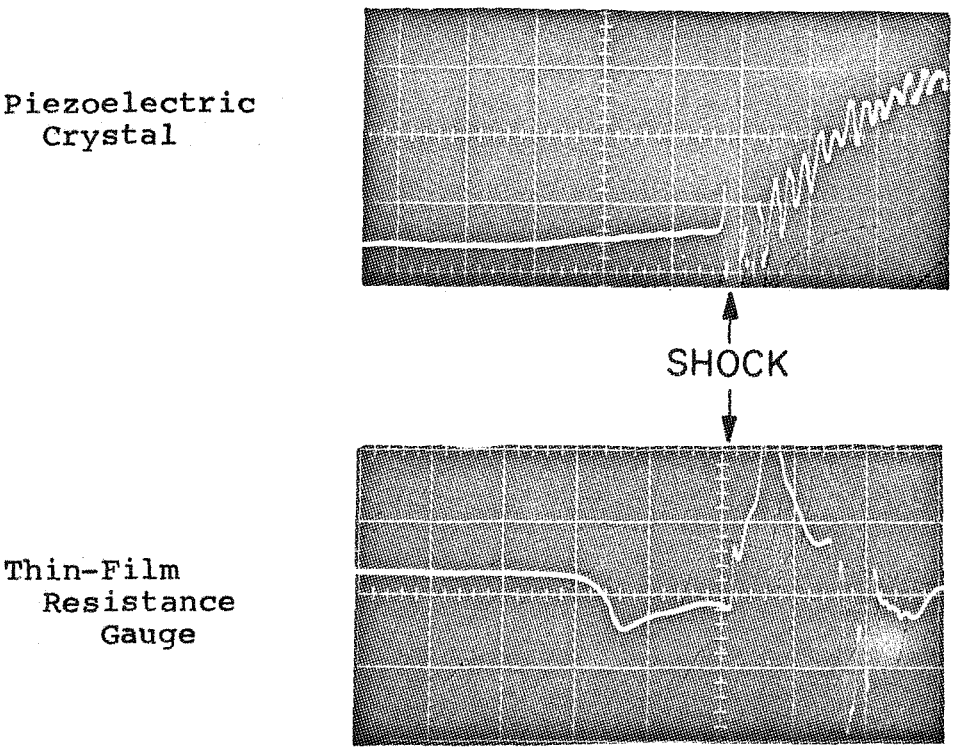

Sweep Rate: 20 μsec/div (left to right)

Figure 21. Typical Piezoelectric Crystal and Thin-Film Resistance Gauge Oscillograms

Conditions: P_1 = 0.120 torr xenon
M_s = 18.5

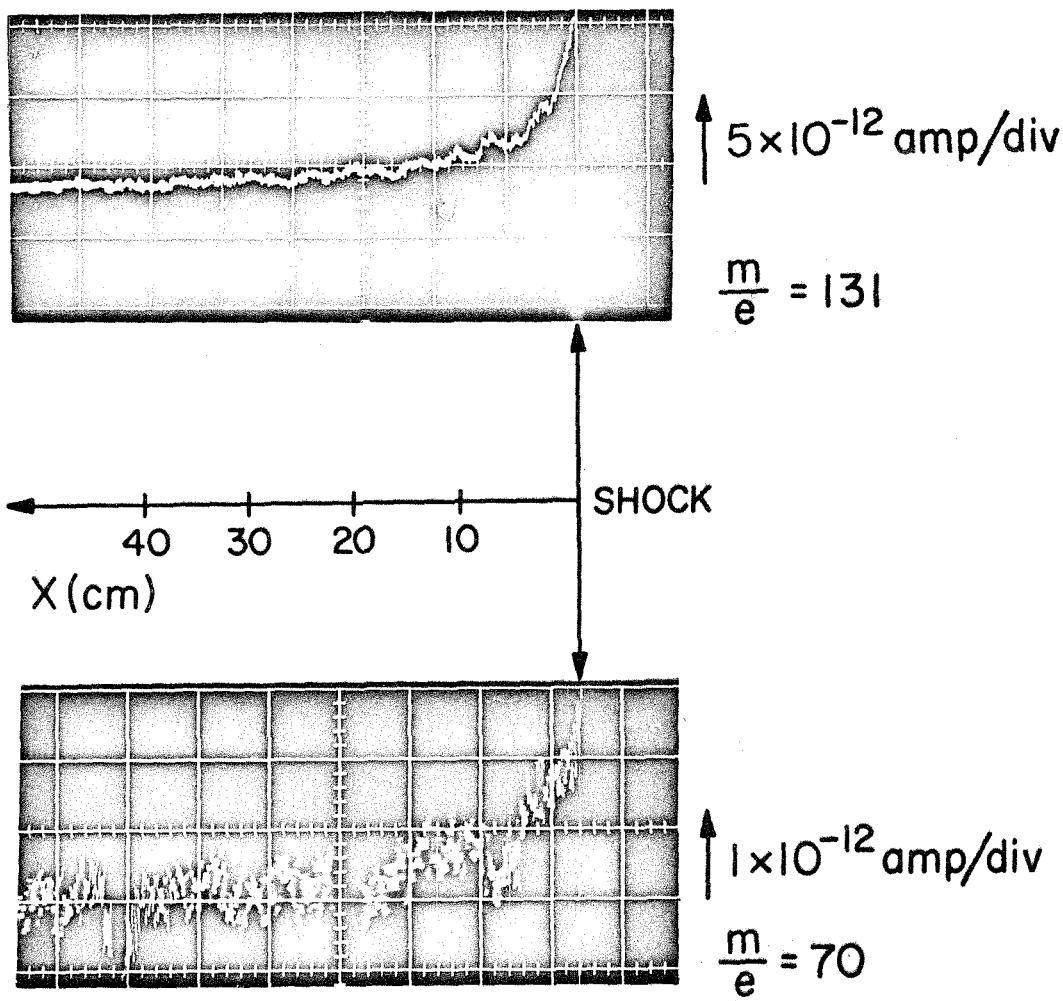

Figure 22. Typical Spectrometer Oscillograms Showing the Method of Data Reduction

Sweep Rate: 20μs/div

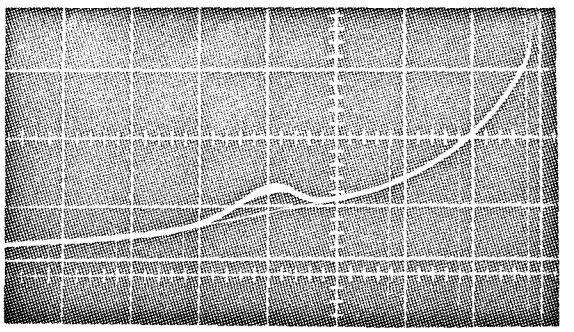

10 mv/div

20 μsec/div

Figure 23. Typical Double Probe Response Showing Localized Perturbation

Conditions: P_1 = 0.100 torr xenon

M_s = 19

Type D Preamplifier
Type 555 Oscilloscope

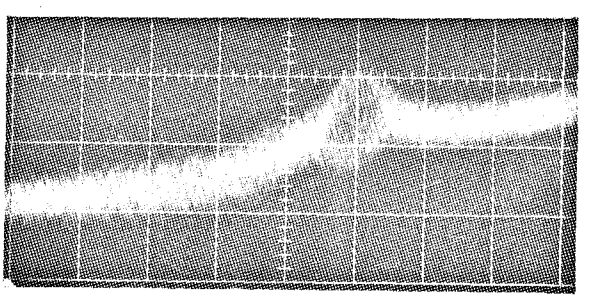

5 mv/div

10 μsec/div

Figure 24. Double Probe Response Showing Localized Perturbation with Fast-Rise-Time Circuitry

Conditions: P_1 = 0.100 torr xenon

M_s = 19

Type 10A1 Preamplifier
Type 647A Oscilloscope

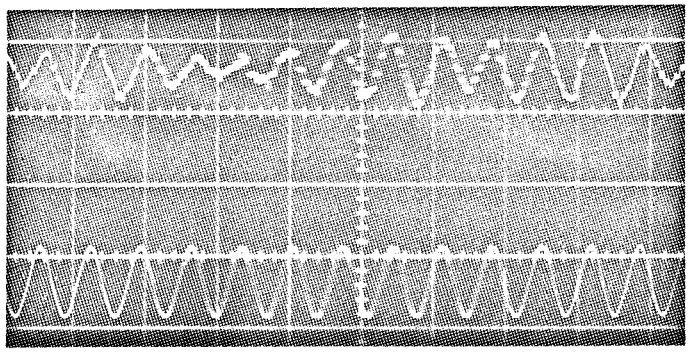

Shock Tube

1.3 MHz
Reference

Figure 25. Shock Tube and Associated Equipment
Ground Reference

Sensitivity: 100 mv/div
Sweep Rate: 1 μsec/div

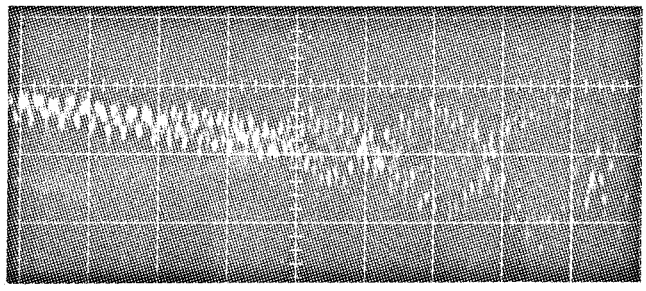

1 mv/div
1 μsec/div

Figure 26. Detail of Probe Perturbation Showing Modulations and High Frequency Components

Conditions: P_1 = 0.120 torr xenon
M_s = 18.5

Type 10A1 Preamplifier
Type 647A Oscilloscope

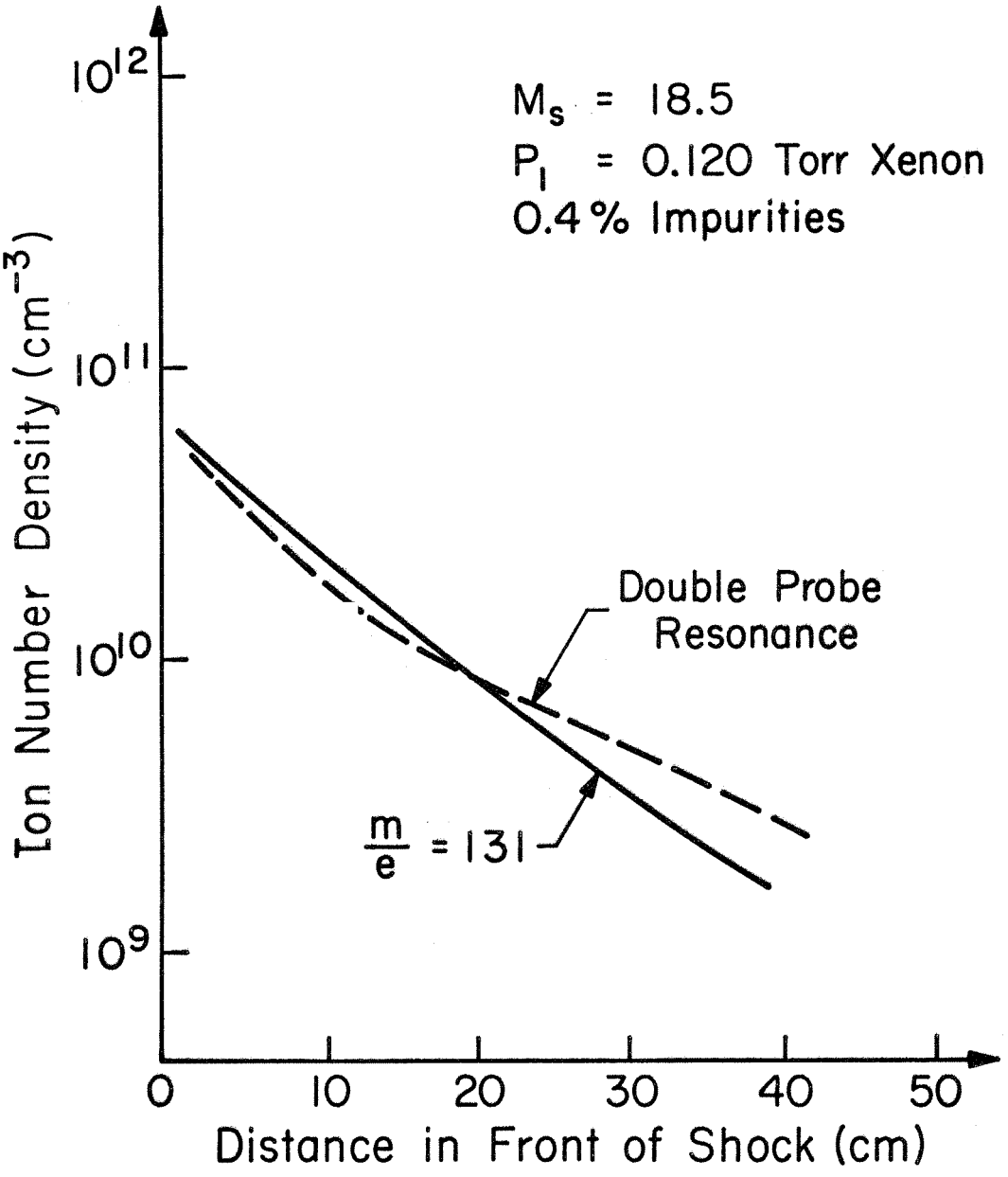

Figure 27. Comparison of Spectrometer Current Using Semi-Empirical Calibration and Probe Current Using Ion Resonance as Reference